Materials & Design 243 (2024) 113031

Contents lists available at ScienceDirect

Materials & Design

journal homepage: www.elsevier.com/locate/matdes

Automated segmentation of large image datasets using artificial intelligence for microstructure characterisation and damage analysis

Setareh Medghalchi [a,*], Joscha Kortmann [a], Sang-Hyeok Lee [a], Ehsan Karimi [a], Ulrich Kerzel [b], Sandra Korte-Kerzel [a]

[a] *Institute for Physical Metallurgy and Materials Physics, RWTH Aachen University, Aachen, Germany*

[b] *Data Science and Artificial Intelligence in Materials and Geoscience, Fakultät für Georessourcen und Materialtechnik, RWTH Aachen University, Aachen, Germany*

ABSTRACT

Many properties of commonly used materials are driven by their microstructure, which can be influenced by the composition and manufacturing processes. To optimise future materials, understanding the microstructure is critically important. Here, we present two novel approaches based on artificial intelligence that allow the segmentation of the phases of a microstructure for which simple numerical approaches, such as thresholding, are not applicable: One is based on the nnU-Net neural network, and the other on generative adversarial networks (GAN).

Using scanning electron microscopy images collected from large areas (~1 mm^2) of dual-phase steels as a case study, we demonstrate how both methods effectively segment intricate microstructural details, including martensite, ferrite, and damage sites, for subsequent analysis.

Either method shows substantial generalizability across a range of image sizes and conditions, including heat-treated microstructures with different phase configurations. The nnU-Net excels in mapping large image areas. Conversely, the GAN-based method performs reliably on smaller images, providing greater step-by-step control and flexibility over the segmentation process.

This study highlights the benefits of segmented microstructural data for various purposes, such as calculating phase fractions, modelling material behaviour through finite element simulation, and conducting geometrical analyses of damage sites and the local properties of their surrounding microstructure.

1. Introduction

Almost all materials used in today's applications are produced and tailored using specific production processes, meaning that their properties do not only depend on the chemical composition, but, in particular, on the microstructure that is formed from the various phases, their size and morphology, crystal orientations and lattice defects in the material. Much of materials science research is, therefore, focused on understanding the properties that emerge from the microstructure and how to develop tailored processing chains to obtain materials with well-controlled microstructural variables yielding desirable properties. To be able to understand the relationship between the microstructure and the properties of the material quantitatively, one continuing challenge is to accurately describe the microstructure regarding the phases and phase fractions, as well as their geometries [1]. Such a representation does not only enable comparisons of different materials or assessment of processing success, it also forms the basis of computational analyses or studies of microstructure evolution during straining, heat treatment [2], welding [3], or other exposure to different environments [4].

The domain of microstructure modelling and design typically uses a limited set of variables or descriptors to represent the microstructure on three levels: i) composition (comprising phases and their volume fractions), ii) dispersion (discriminating between distinct microstructural components), and iii) particle phase geometry (can include phase attributes like size, area, and roundness) [1]. However, it is important to keep a balance as excessive simplification by limiting the number of descriptors or uncertainty in their quantification may lead to loss of physical significance [4]. In the past century, materials science has made substantial progress in acquiring and analysing microstructural images to provide as detailed as possible a view of each material's microstructure [5,6]. Microstructural image segmentation emerges as a pivotal technique, enabling the dissection of intricate visual data into meaningful components [7]. Microstructural image segmentation commonly involves partitioning of a microstructure image into its constituent parts, such as grains [8–13], phases, and defects [14–16], assigning physically meaningful and spatially structured data to its constituents [17,18]. This also enables a direct transfer of experimental data into modelling of microstructural processes or properties, forming a bridge between theory and experiment.

Conventionally, microstructure segmentation is performed manually

---

* Corresponding author.

E-mail address: medghalchi@imm.rwth-aachen.de (S. Medghalchi).

https://doi.org/10.1016/j.matdes.2024.113031

Received 26 February 2024; Received in revised form 30 April 2024; Accepted 16 May 2024

by human experts and supported by a range of numerical approaches such as thresholding [19–22], region growing [23–25], edge detection [26,27], and clustering [28]. In addition, advancing analytical methods assist to automate this process, for example by using correlated micrographs with different electron detectors, giving topographical or chemical contrast, or employing energy dispersive spectroscopy (EDS) or electron backscatter diffraction (EBSD) inside the scanning electron microscopy (SEM) to capture more explicitly distinguished phases and grains. However, this type of analysis, while providing a wealth of information and high spatial resolution, is again time- and resource-consuming and rarely scaled to areas representative of a finished or semi-finished product. Lately, machine learning and increasingly automated imaging equipment are emerging to bridge this gap in scale [29,30]. These methods enable analysis of large datasets, such as from synchrotron tomography [31–33], X-ray tomography [34], micro-computer tomography (CT) [32] and optical or electron micrographs [33,35,36], and have been adopted for different purposes including feature detection and classification [29,30,37,38] and microstructure segmentation [32,34–36,39,40]. Using images recorded at different scales, from light optical microscopy (LOM) to high resolution transmission electron microscopy (HR-TEM) [41], objects or phases of interest have been segmented in various microstructures, for example, including ferrite, martensite, cementite particles and lath shaped bainite in different grades of steels [39,42–46], or γ' precipitates, dendrites [34] and their cores [47] in nickel based superalloys [48–50].

However, a lot of these methods do not easily scale to much larger datasets. This is particularly challenging where the size of the dataset can be successively increased by merging adjacent datasets. Typical challenges then include the handling of the large dataset itself and dealing with variability in the underlying data, e.g. as a result of changes in focus, contrast or brightness during imaging or fluctuations of the sample thickness or surface quality from sample preparation. This variability impedes the collection of homogeneous image data, making conventional image segmentation methods less applicable, as these methods are typically tailored to specific image properties, such as brightness and contrast, and may struggle to adapt to image variations [31,32,41].

In this work, we present two novel approaches for microstructure segmentation based on artificial intelligence, one method is based on generative adversarial neural networks (GAN), and the other on nnU-Net. We employ both methods on scanning electron microscopy images collected across large areas ($\sim$1 mm^2) to reveal features of sub-micron scale across images that span hundreds of micrometres (μm) in either direction. As our sample material, we image a commercial dual phase steel (DP800). This type of steel is used extensively in a wide range of commercial applications, particularly in the automotive industry [51,52], and improvements in this material have direct impact on many production processes and their applications [2,7,53,54]. It also has a rich multi-phase microstructure that is formed during sheet processing and tailored to sustain large mechanical strains before failure. The final microstructure of the as-processed or subsequently strained material contains features ranging from small voids reaching the resolution limit of scanning electron microscopy to large martensite bands undulating at a shallow angle along the sheet material and giving rise to strong variations in the microstructure observed in sections taken parallel to the sheet itself [30,38]. Furthermore, unlike many other materials containing multiple phases [55], the two major constituent phases of the dual phase steel, the brittle martensite and much more ductile ferrite phase [56], appear very similar in scanning electron microscopy and therefore provide an adequate challenge for segmentation where simple thresholding, for example, fails across large images.

In addition to a brief introduction to the two segmentation methods employed here and their application to the dual phase DP800 steel, we will present examples of how segmented microstructural data of large images can be used for subsequent analyses. Three aspects will be considered in these examples: (1) the apparently simple task of determining the phase fraction across a microstructure of large variability at different scales, (2) the use of segmentation to extract core geometric features after manual or neural network-based classification, and (3) the use of a large segmented dataset to enable modelling of a large number of features of different type and size that correspond to a real, deformed microstructure. In Fig. 1, a summary of the approaches and examples in this work is given.

2. Introduction to the implemented segmentation methods and materials

2.1. Artificial intelligence for image segmentation

In order to analyse a microstructure in detail, we need to be able to attribute each part of the micrograph to a specific feature of the image, in our case either a martensite or ferrite phase, or a void introduced as damage during mechanical straining. On an abstract level, we, therefore, want to use a machine learning algorithm to “translate” an input image to a suitable output image showing which phase or damage is where. In our case of the DP800 steel, the input image is the grayscale electron micrograph obtained from a scanning electron microscope, and the desired output image shows, pixel by pixel, whether a given pixel originates from the martensite phase, the ferrite phase, or a damage site. This process is called segmentation, and we distinguish between instance and semantic segmentation: In semantic segmentation, we attribute each pixel in an image to a pre-defined class, such as martensite, ferrite, or damage. Instance segmentation goes beyond semantic segmentation and aims to identify each object uniquely with its associated segmented pixels, such that each object can be referred to separately [57,58]. In this work, we focus on semantic segmentation and will refer to semantic segmentation and segmentation synonymously throughout the text.

The training data for the machine learning based approaches used in this work were experimental images, obtained by manually labelling scanning electron micrographs, using the Pixel label option of the Image Labeler application of MATLAB 2018a [60]. This tool provided the most precise labelling possibility at the time of preparing this data. Fig. 2 shows an example of the raw (left) and labelled (right) image. Each image in the training data has a size of 512 × 512 pixels that corresponds to a resolution (number of pixels per length), of 32 pixels/μm. In total, we have labelled 171 SEM images. The labelling of the ground truth data primarily serves the purpose of defining the phases. It involves the manual process of successive clicking around specified phases, namely martensite and damage sites, within the ferrite matrix. However, certain minute details, such as extremely thin martensite islands or remnants of colloidal silica suspension (OPS) particles resulting from the metallographic preparation, that lack significant physical relevance to the material’s properties, are excluded from this process to alleviate the effort. The orange arrows in Fig. 2 indicate a few of these cases.

2.1.1. nnU-Net

The UNet architecture of convolutional neural networks [61] was primarily designed for image segmentation in biomedical images. It consists of a contraction part based on convolutional neural networks that learn the abstract features in the image, a “bridge”, and an expansive part that then creates the output image. So called “skip connections” between the contraction and expansive parts convey information about specific features across the network topology. The name UNet originates from the U-like shape of the setup after the skip-connections between the contraction and expansive part are introduced [62]. This approach has been widely used for various computer vision tasks. Its efficient use of parameters allows the training on a limited number of training data or devices with few resources [59,61,63,64].

The most recent variant is nnU-Net (“no new UNet”) [63], which extends the original UNet approach to include automatic configuration, including the pre- and postprocessing of the data, the network

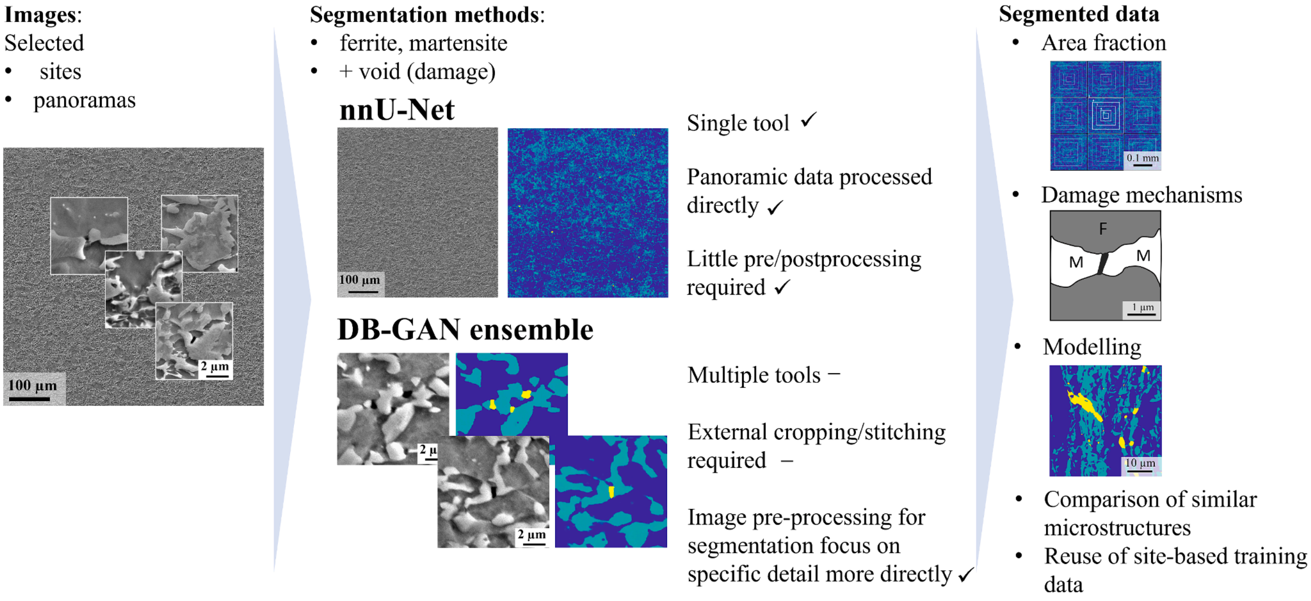

Fig. 1. Two approaches for automatic segmentation of the microstructural images with the corresponding benefits of segmented data.

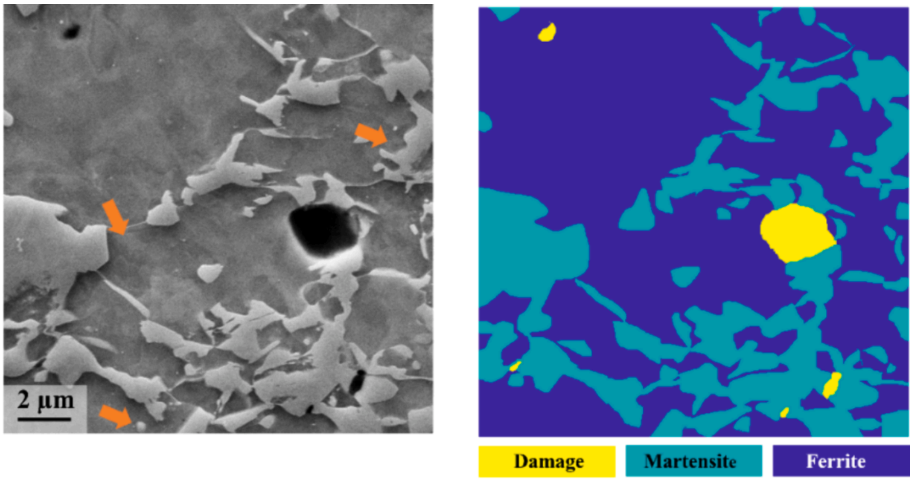

Fig. 2. Example of the manually labelled ground truth data with different colours for ferrite, martensite and damage sites. Orange arrows indicate some minute details which have not been manually marked.

architecture, and the network training, thereby alleviating many of the difficult and tedious tuning steps required in most neural network-based approaches. The postprocessing can include, for example, the removal of artifacts or smoothing of edges [65,66]. To avoid the risk in our application of this method for the analysis of dual phase steel that damage sites or small martensite island may be removed, we decided not to apply any post-processing in this work.

The overall workflow used to tune and train the nnU-Net in this work is illustrated in Fig. 3. The nnU-Net approach uses three classes of parameters: Fixed parameters, rule-based parameters, and empirical parameters. The fixed parameters have been tuned by the developers of the algorithm and are not changed in many applications. However, following the work by Isensee *et al.* [67], we also vary these fixed parameters here. The rule-based parameters are optimised automatically using heuristics that are extracted using a “dataset fingerprint”, calculated for each new dataset the network is being trained on. These parameters include, for example, the network topology, batch size, etc. The empirical parameters must be tuned manually.

The default values of the fixed parameters include: the architecture template (UNet), the choice of optimizer (here, stochastic gradient descent is employed, following the methodology presented in the original work [63] and the findings of [68]. In a previous study [68], higher generalizability is observed with stochastic gradient descent in comparison to adaptive methods), the learning rate schedule (starting from 0.01, following $l_r = (1 - \frac{e_p}{e_{p,max}})^{0.9}$ where e_p is the current epoch and $e_{p,max}$ is the total number of epochs), the training schedule (1000 epoch are defined as, each epoch completes 250 training batches), the choice of loss function (cross entropy) [69], and the default data augmentation (rotations, scaling, Gaussian noise, Gaussian blur, brightness, contrast, simulation of low resolution, gamma correction and mirroring).

In total, we have 171 experimental images (512×512 pixels images with 32 pixels/µm resolution), that we split as described in the following, depending on the training scenario. To be able to test the trained network on an independent dataset that was not seen by any network during training, we set seven of the experimental images aside for this purpose. The remaining images were split such that 131 are used for the training of the network (the training dataset) and 33 images for independent evaluation in all cases except for the cross-validation. These 33 images form the validation dataset. In all cases but the cross-

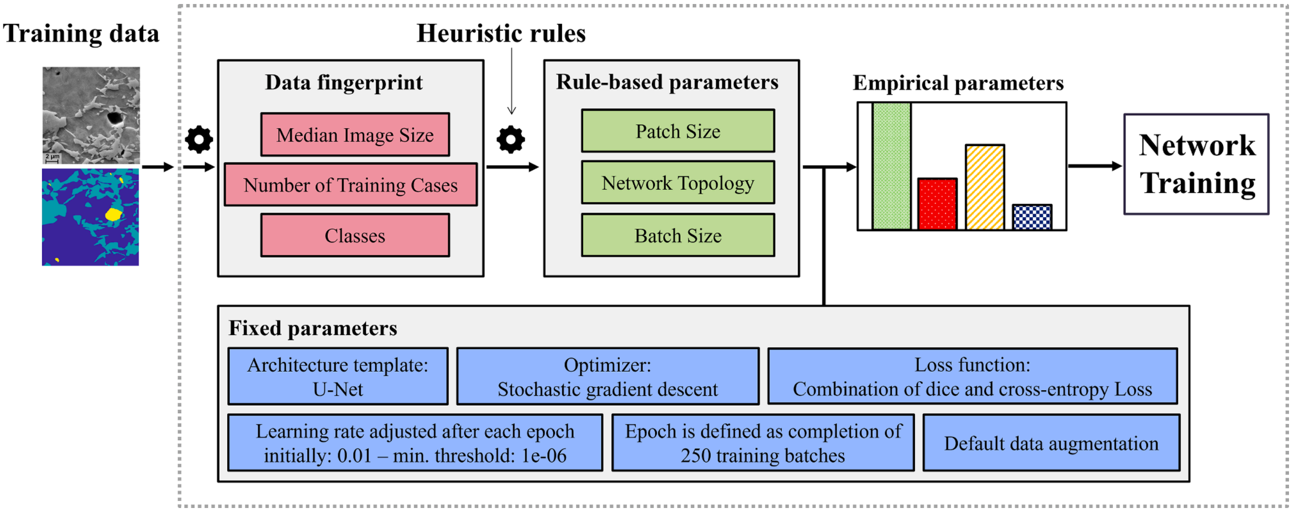

Fig. 3. The adapted and simplified flowchart of the nnU-Net method, based on [67], for the current dataset.

validation approach, the images that form the validation and training dataset are chosen randomly before training any of the networks and are kept fixed for all network configurations. For the case of cross-validation, 131 plus 33 images (i.e. the training and validation dataset) are given to the network and the cross-validation procedure then randomly chooses the split between the training and validation data using the same ratio as in the other cases. As mentioned above, the seven images in the test dataset are not seen by any network during training.

Additionally, we investigated the following changes to the fixed parameters:

- Data split: We explored different data split strategies, with 5-fold cross validation [67] and fixed validation set, and augmentation of the training data (up to 987 training data). The data augmentation techniques applied here are a translation operation, flip operation, rotation operation of 90° and 160° and a shear operation.
- Loss function: Apart from Dice and cross entropy loss (CE) in the original work, following some medical image segmentation approaches, we have explored other loss functions. Here a combination of TopK loss (TopK) and dice loss (Dice) have been explored besides CE [70].

Heuristic rules in correlation to the hardware capabilities (e.g., GPU memory), define the rule-based parameters. These parameters for our data are: batch size (8,12), patch size (median image size, 512 × 512 pixels) and the network topology (like the number of down sampling layers). Fig. 4 illustrates the different sets of experiments explored while tuning the network parameters.

The segmentation of the images with sizes larger than the training data is done by using a sliding window [63]. Specifically, the network rasters across the image and segments it into windows of the same size as the patch size utilised during the network's training, here 512 × 512 pixels. There is an overlap of half the patch size between the neighbouring predictions. The predictions are combined by averaging the softmax outputs of the network across all predictions. The accuracy diminishes towards the edges of individual predictions due to the padding applied in convolutions. To avoid stitching artifacts, Gaussian importance weighting is applied to the resulting prediction, assigning higher weights to the canter voxels during softmax aggregation [63].

Training the network was performed on central high-performance computing facilities of RWTH Aachen university, with a GPU node providing a Nvidia Tesla V100 graphics card, and 16 GB RAM, as well as 1 TB storage.

2.1.2. *Generative adversarial networks*

On a high level, GAN [71] consist of two competing networks: One network, the generator, is used to create realistic images, and the other, the discriminator, tries to tell the generated image apart from real

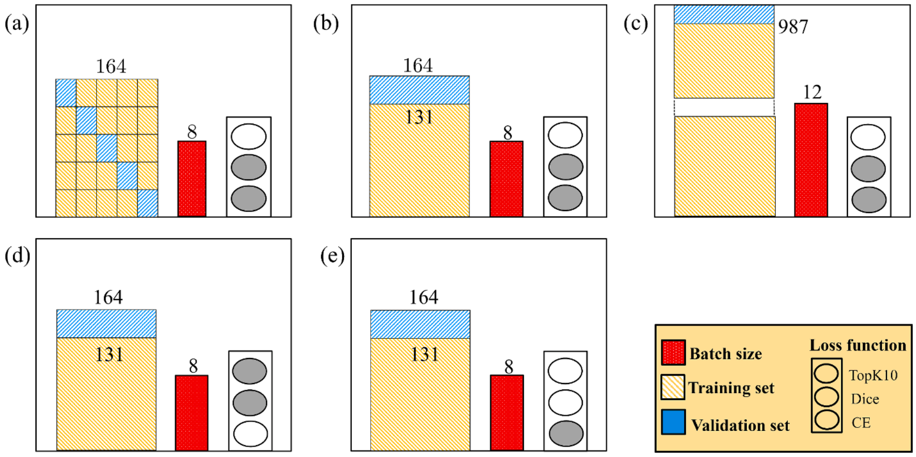

Fig. 4. A) data split: 5-fold cross validation, loss function: dice + CE, b) fixed validation set, loss function Dice + CE, c) training data augmentation, loss function: Dice + CE, d) fixed validation set, loss function: TopK + Dice, e) fixed validation set, loss function: CE.

images. The training of the generative adversarial network stops when the discriminator network is no longer able to tell the “fake” generated images apart from real images. More formally, GANs learn the mapping from a random noise vector z to some output image y: $G: z \rightarrow y$. A variant, the conditional GANs (cGAN) [72], allows conditioning on a quantity of interest in the image generation process. Building on this approach, pix2pix GANs [73] use images for the conditioning, such that this kind of network learns the mapping from an image x and the random noise vector z to some output image y: $G: \{x, z\} \rightarrow y$. This approach allows the “translation” of images, such as, for example, turning black-and-white images into colour images. In our case, we can use this to train the network to produce segmented images from the (raw) scanning electron micrographs by providing a set of already segmented images as part of the training process. A generic workflow of image segmentation using this method is shown in Fig. 5.

We found that cutting the 512 × 512 pixel images into four times as many smaller images gave a higher performance in terms of accuracy for the GAN-based method. We elected to use images of size 250 × 250 pixels (corresponding to 32 pixels/µm) during network training, rather than 256 × 256 pixels, to enable compatibility with previously collected images [30,37,74], allowing for a seamless application of the final trained network. In total, 656 of such images were created as training and test data from the fully labelled ground-truth images described above. We achieved this by dividing each of the original 164 images into four smaller images, resulting in a total of 656 images, with slight resizing applied to transform between 256 x 256 and 250 x 250 pixels image sizes. We used a batch-size of 10 and a learning rate of 0.0002 during the training process and trained the network for 150 epochs. The choice of the batch size in both methods was a trade off with respect to the hardware capabilities and method performance.

Visually, the segmented image output from the pix2pix GAN, includes artifacts that mostly affect the ferrite and martensite islands (Fig. 6b). Therefore, we propose and include here the following procedure as a postprocessing step to improve the quality of the segmented image: Similar to the work in [30], we use the DBSCAN clustering algorithm [75] to identify clusters of pixels that can be attributed to damage. Typically, damage appears as an agglomeration of black pixels in the electron micrograph. However, due to the imaging process, the black level varies across all damage sites on the micrograph, meaning that we cannot use a single colour threshold. Therefore, we used the dynamic colour thresholding algorithm, Yen [76], to separate the black pixels. Next, the DBSCAN algorithm was applied to detect the islands with black pixels specifically in the microstructure. The use of DBSCAN algorithm often results in the exclusion of very small clusters (noises) of black pixels which do not actually form voids. Nonetheless, some small black voids are detected in this step, for example shadows (Fig. 6c). Therefore, in a subsequent step, only the damage sites predicted by both pix2pix GAN and DBSCAN are selected to remain in the final images (Fig. 6d). The damage sites identified by both methods (yellow clusters in pix2pix and black clusters in DBSCAN result), represents a proper alternative to actual damage sites. However, the ferrite and martensite masks retain some artefacts like open islands or dispersed pixels of martensite on the ferrite island (some examples shown by orange arrows in Fig. 6e). Finally, a morphology correction step, was applied to clean the dispersed noises (cleaning) and a closing operation was applied on top of that to fill the open islands of martensite where some missing pixels exist (Fig. 6f). Due to the combination of the methods applied here, we call this method “DB-GAN ensemble” within this work.

Therefore, the overall workflow is similar to the one for the nnU-Net based approach: The large-scale panoramic images need to be cropped to smaller patches of the same size as the training data, the segmentation and postprocessing procedure is then run, and, finally, the smaller images are stitched back together to obtain a larger image. However, while this approach is fully automated in case of nnU-Net, this has to be done separately by the user in case of the GAN based approach. Furthermore, as mentioned above, better performance was obtained using images of size 250 × 250 pixels as training data for the GAN based approach, meaning that many more cutting/stitching operations are needed compared to the nnU-Net based approach. An example of this process is shown in Fig. 7. This additional cutting and stitching step can introduce additional artefacts that are not present in the nnU-Net-based approach as the latter can handle much larger images by the sliding window approach. In principle, a sliding window approach could also be implemented for the GAN-based analysis. However, as this requires not only the method itself but also rules for dealing with differences in the overlapping areas, we have refrained from implementing this additional step with a few to avoiding additional and more difficult to interpret artefacts.

2.2. Material and experimental methods

Damage in dual phase steels occurs as a result of different deformation mechanisms at the microscale within and between the two constituent phases [52,77]. The propensity of dual-phase (DP) steels to

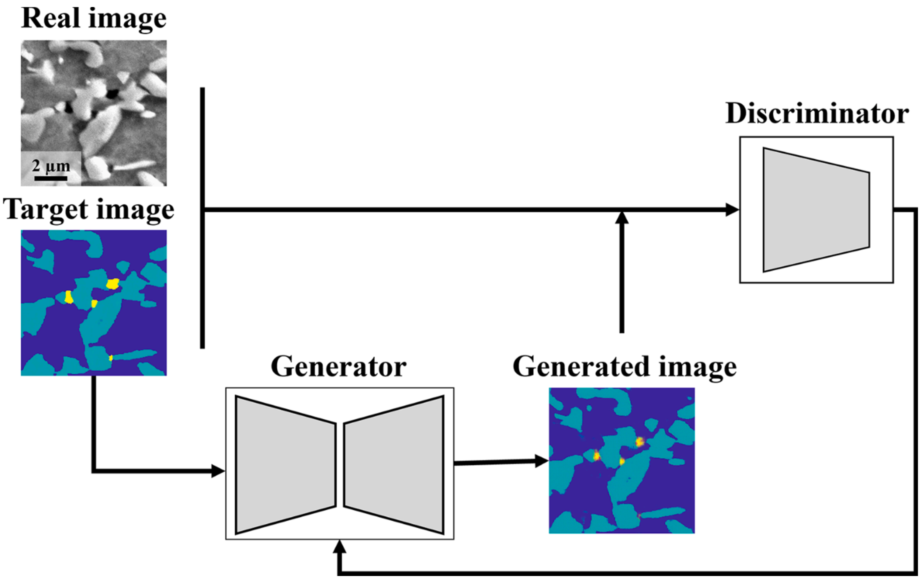

Fig. 5. Generic workflow of image segmentation by the pix2pix GAN.

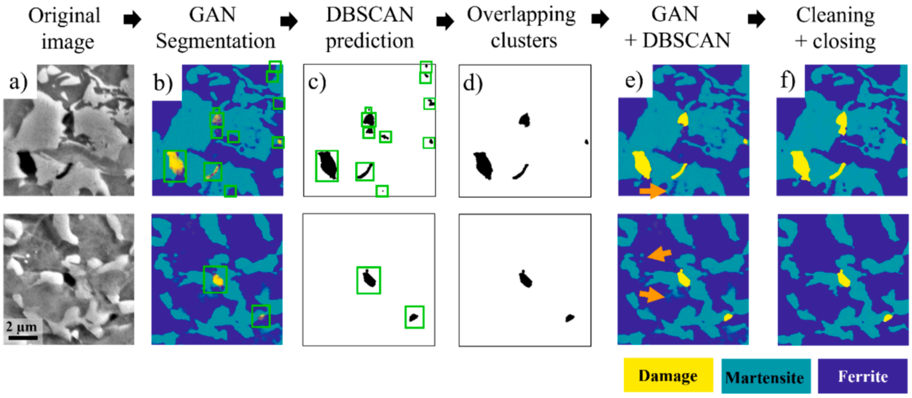

Fig. 6. Step by step representation of the DB-GAN ensemble method. a) Original SEM image, b) segmentation result of pix2pix GAN, c) the damage sites identified by the DBSCAN clustering algorithm, d) the damage sites identified by both DBSCAN and pix2pix GAN, e) overlay the results of pix2pix and DBSCAN, f) the result after the morphological corrections by closing and cleaning. Orange arrows indicate the artifacts of pix2pix GAN.

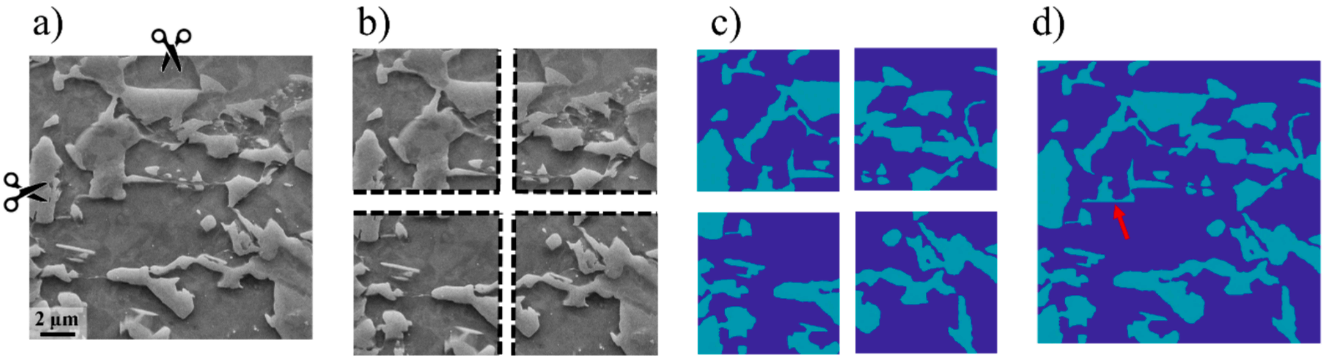

Fig. 7. A) sem image with size 512 × 512 pixels, b) 4 images of size 250 × 250 pixels images cropped and resized to the size of the training data, c) application of the DB-GAN ensemble method, d) stitched, segmented image. The red arrow indicates the error introduced due to cropping and stiching.

incur damage and failure during quasi-static testing is strongly correlated to the local microstructural characteristics giving rise to local internal strains [78,79], and has a pronounced impact on the fracture toughness [80–85] and fatigue crack growth resistance [81,86,87]. Important microstructural features therefore include those associated with the properties of the individual phases, such as the martensite carbon concentration [88], martensite internal structure [89], hardness of martensite [90], and strain hardening capacity of the ferrite [91], or their morphology within the dual phase microstructure, characterised by the volume fraction of the martensite phase [88,92–94], and the morphology of the ferrite grains and martensite islands [95–97], the microstructural morphology, the grains' or islands' size and aspect ratio, and the interconnectivity [98]. Furthermore, the nucleation and evolution of deformation-induced damage naturally depend on the amount and direction of applied strain, and any changes in the strain path [30,37,38]. These in turn give rise to the heterogeneous local strain distribution originating from the two phases' mechanical contrast, as revealed by high-resolution microscopic-digital image correlation (µDIC) and crystal plasticity (CP) simulation [99,100].

The strong interest in dual-phase steels has already attracted considerable interest in microstructure analysis [101–104], particularly in terms of phase segmentation. EBSD-based approaches are typically challenging for this kind of material, since the crystallographic relationship between the two phases (ferrite and martensite phase with BCC and BCT crystal structures, with small tetragonality in the martensite phase) is very close, and phase separation becomes even more challenging where the internal strain is high, i.e. particularly after deformation.

Martinez Ostormujoj et. al. [46] combined orientation information collected from EBSD and its associated kernel average misorientation (KAM) and pattern quality maps using a UNet segmentation algorithm [61] for this phase segmentation, however, the approach lacks decent transferability from the pristine, undeformed material to deformed samples with high internal strains.

Most alternative methods that allow distinction of such similar phases either possess comparatively low spatial resolution, such as X-ray diffraction using typical laboratory setups, or are confined to relatively small areas or volumes, like transmission electron microscopy (TEM). In contrast, the large variability of the microstructure mandates the extraction of phase assignment at sub-micron level of individual martensite islands and damage sites, but across large scales to capture the commonly encountered martensite banding. High resolution, segmented data across large areas of the order of at least 1 mm^2 is, therefore, essential to be able to represent the microstructure in subsequent analyses or modelling in a meaningful way. Here, we present a method that is capable of segmenting panoramic images acquired in the SEM that resolve sub-micron features across an area of the order of a mm^2 without requiring diffraction information or conditions or clear grey-scale separation of the two phases after etching.

To image and segment a common and at the same time challenging microstructure, we used a commercial DP800 dual-phase steel (ThyssenKrupp Steel Europe AG) with a tensile strength of the order of 800 MPa. The chemical composition and mechanical properties of this steel can be found in [105]. Samples were cut out of a 1.5 mm thick sheet metal into dog bone shaped tensile specimens and then elongated uniaxially in the rolling direction specified by the manufacturer. The tensile tests were performed using a microtensile stage (Proxima 100; Micro-Mecha SAS, France) with a gauge length of the tensile samples of 3.65

mm and a square cross-section of 1.5 mm side length. After testing, the samples were cut to the gauge length with an electron discharge machine and were deformed to different elongations (14 %, 19 %, and 25 % engineering strain). By using different levels of deformation, damage sites of different density, size and dominant underlying damage mechanism are included in the training data.

The initial surface was prepared by grinding the surface manually using sandpapers starting from 800 to 4000 grit. Afterwards, the samples were polished mechanically with 6 μm, 3 μm, and 1 μm diamond suspension with an alcohol-based lubricant (99.5 % Ethanol + 0.5 % Polyethylene Glycol), and final polishing and cleaning was performed using colloidal silica suspension (OPS). Finally, each sample was subjected to a 1 % Nital solution for 10 s, leading to a visible phase contrast between ferrite and martensite in the electron microscope due to preferential etching of the ferrite phase. A typical microstructure of this steel after etching is shown in Fig. 8 in plane-view and cross-sectional view. Typically, martensite islands are visible in light grey, while the ferrite matrix is darker grey, and deformation-induced damage appears as voids in black. The banded martensite is visible directly in the sheet cross-section (Fig. 9a), and indirectly in the variable martensite density in plane-view. Typical deformation induced damage sites [38] are shown inset at higher magnification.

To collect high resolution images from large areas of the microstructure (around 1 mm^2), panoramic imaging was conducted using scanning electron microscopy (SEM). For this purpose, a sequence of individual high-resolution images (32 pixels/μm) each measuring 100 μm × 100 μm, were collected with 20 % overlap between the adjacent images. The stitching of these windows was performed using the Image Composite Editor 2.0.3.0 software.

3. Results

3.1. nnU-Net

The resulting network topology for the corresponding SEM images of the DP800 dual phase steel is illustrated in Fig. 9. After the automatic optimisation of the rule-based parameters using the dataset fingerprint, the final nnU-Net topology consists of seven down-scaling operations, and the network is initialized by 32 feature maps at the first place and then increasing to 480 at last. Finally, the down sampling operation is terminated when the feature map results in size 4 (at the bottom row) continued symmetrically by up-scaling operations.

From the different packages of experiments, the package with a fixed validation set and with (CE + Dice) loss function was selected. This package achieved 96.2 % and 82.9 % for validation accuracy and dice score respectively on the test set, (marked with red box in Fig. 10). The evaluation metrics of all packages of conducted experiments and the respective values for the individual classes for the selected package are also given in Fig. 10. The validation dataset refers to the average of the splits into training/validation data chosen automatically during the cross-validation approach, and, for the other cases, to the fixed validation dataset consisting of 33 images chosen randomly before the training of any package starts.

The quantitative evaluation of the results, based on pixel-by-pixel comparison, did not show significant differences for the various packages. However, the package associated with a fixed validation set (highlighted by the red rectangle in Fig. 10) exhibited the best visual performance on both the test and validation sets, according to the judgment of material scientists. In particular, better visual performance judged by human experts involved replication of fine details in the microstructure, such as thin protruding pixels from larger islands or thin connecting segments between islands. Although here the images chosen for the validation set are arbitrary, opting for the package with 5-fold cross-validation might be a prudent choice to try in other experiments, due to the mixed nature of the data split, favouring unbiasedness.

3.2. DB-GAN ensemble

For the evaluation of the microstructural images segmented by the GAN and DB-GAN ensemble method, we calculated the average confusion matrix over ten confusion matrices from ten randomly selected test 250 × 250 pixels images. These images were randomly cropped from 512 × 512 pixels images that were excluded from the training data. The segmented images generated by pix2pix GAN and DB-GAN were compared with manually labelled data. Specifically, each pixel in the segmented images was compared with its counterpart in the manually labelled image. The results are depicted in Fig. 11. As shown in this figure, the performance of the GAN method was much improved following the addition of DBSCAN clustering and morphology correction.

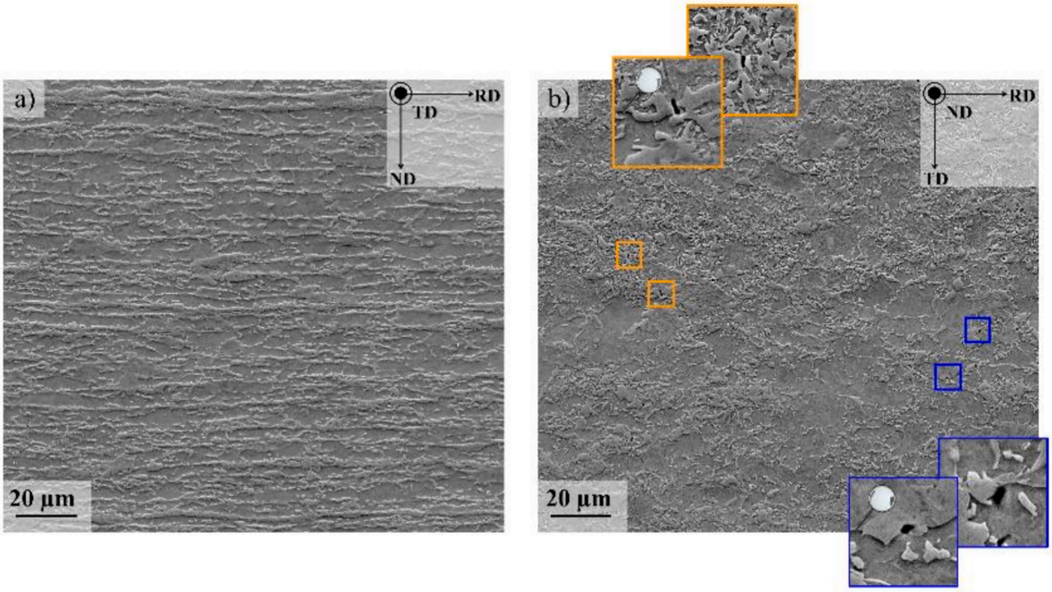

Fig. 8. Micrsotructure of the DP800 steel: a) cross-sectional view revealing banded martensite and b) in plane-view with magnified examples of the two main mechanisms of deformation-induced damage inset (orange: martensite crack, blue: interface decohesion).

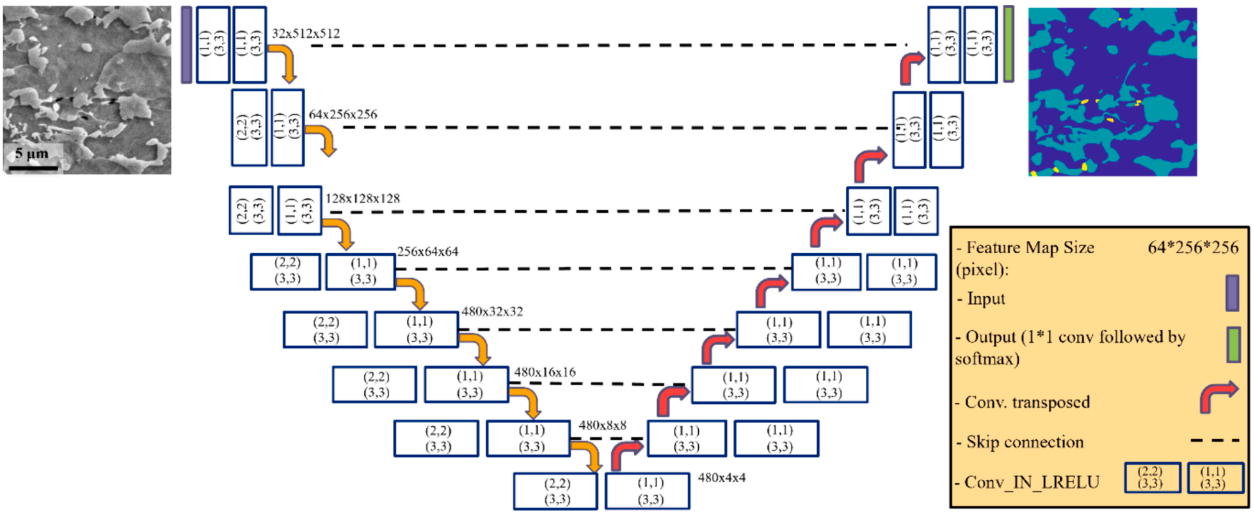

Fig. 9. The optimized U-Net topology for the data.

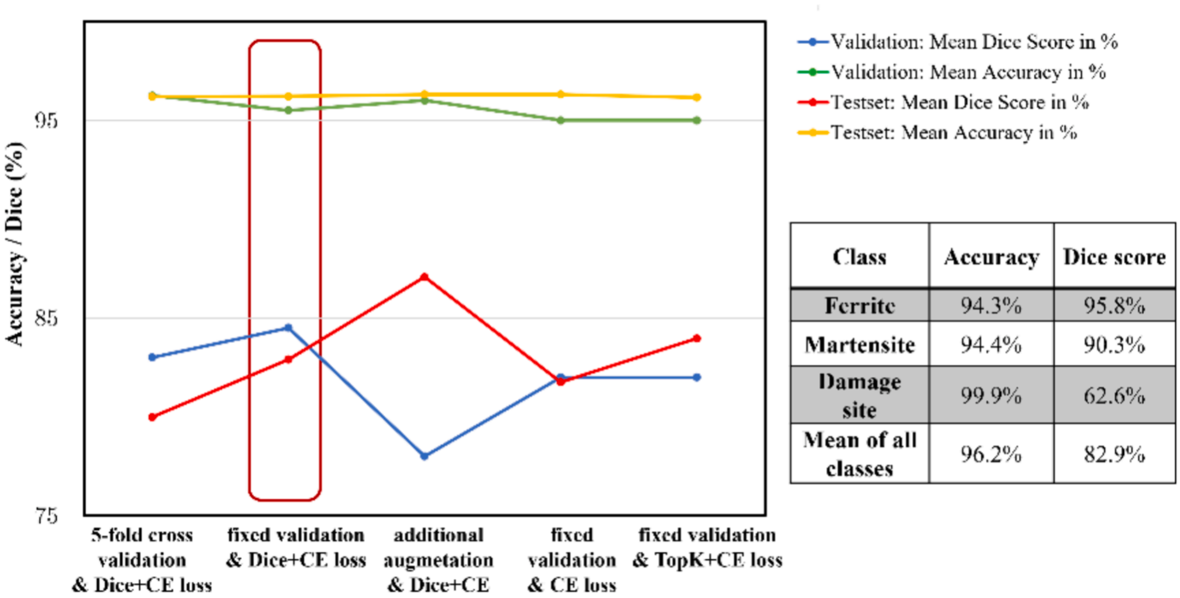

Class	Accuracy	Dice score
Ferrite	94.3%	95.8%
Martensite	94.4%	90.3%
Damage site	99.9%	62.6%
Mean of all classes	96.2%	82.9%

Fig. 10. Evaluation metrics. Accuracy and dice score for the validation and test set for all packages of experiments. The selected package (marked by the red box) possessed the best visual performance. For this case, the related values for each class are also shown in the inset table.

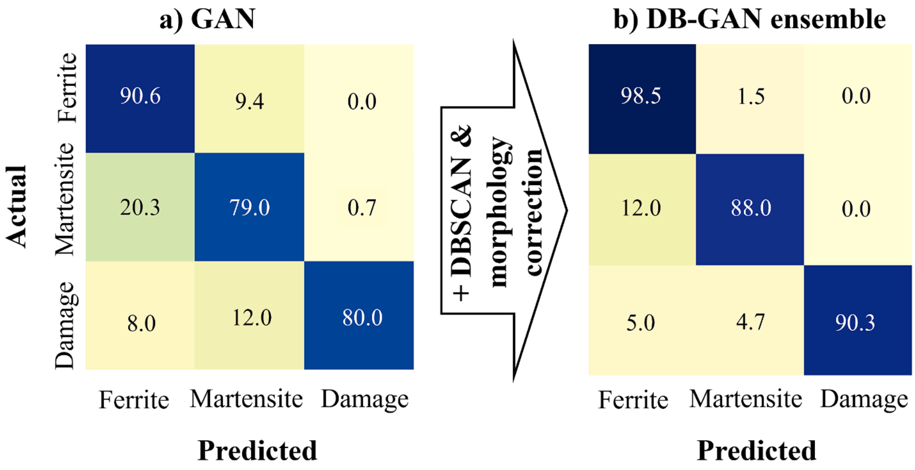

Fig. 11. The average confusion matrix, comparing the performance of the pix2pix GAN and DB-GAN ensemble for ten randomly selected 250 × 250 pixel images.

4. Discussion

Using the example of a commercial DP800 dual-phase steel, we have demonstrated two approaches based on artificial intelligence to segment large panoramic electron micrographs (shown in Fig. 17). The resolution of the images predicted by both methods was consistent with that of the training images (32 pixels/ μm). Here, we discuss first the performance and applicability of the two approaches before highlighting how the information obtained by analysis of such large, stitched micrographs or micrograph arrays can be used for further analyses and investigations.

4.1. *Comparison of image segmentation methods*

4.1.1. *Comparison of the nnU-Net and DB-GAN ensemble methods*

To compare the performance of the DB-GAN ensemble method with the nnU-Net method, we evaluated their performance on two test datasets of images with the size of each method's training data. Each dataset consisted of images that were not seen during training. The images used to evaluation, were of size 512 × 512 pixels for the nnU-Net method and 250 × 250 pixels for DB-GAN method (same set used to evaluate the performance of the GAN based method in Fig. 11). The results are shown in Fig. 12. We observe that both methods exhibit similarly reliable performance.

4.1.2. *Side-by-side comparison of individual features*

Fig. 13 shows a side-by-side comparison of the two approaches for 512 × 512 pixels SEM images with the corresponding ground truth data from manual labelling.

Overall, either approach yields acceptable results, as would be expected based on the similar performance metrics. However, examining the segmented images in comparison to the original SEM images (areas 1 and 2 in Fig. 13c) and Fig. 13d), nnU-Net achieves a higher precision pixel-by-pixel compared to the DB-GAN ensemble approach and is able to preserve finer details of the microstructure in the segmented image. Some of these details can even be related to the remainder of the OPS polishing solution that has not been introduced to the classes and neither labelled in the ground-truth data as it is typically not considered in the analysis of the microstructure. An example of such areas is shown in Fig. 14 with b) and c) showing two different, manually labelled segmentations of the same microstructure. In Fig. 14b), the mask in the ground truth data is not labelled with a pixelwise precision, and Fig. 14c) shows an additional mask applied with a pixelwise precision. This is a typical case where the subjectivity of manually labelled data can introduce uncertainty to the evaluation metrics and the real results. It is evident that the labelling process itself is a source of uncertainty as different experts will, in general, attribute pixels of the intricate features of the microstructure differently to the phases. Nonetheless, some of the fine details have been segmented by the nnU-Net method in Fig. 13c) area 1 and 2. Where the white OPS particles have been segmented, they were identified and segmented as martensite islands. This is unsurprising given that they share the closest colour resemblance to the martensite islands and a separation of the two is challenging for the human eye as well, particularly where agglomerates preclude identification based on spherical shape, as is the case for the largest such particle in Fig. 14.

Similarly, a damage site and a small white island have not been identified by the GAN-based segmentation algorithm (areas 1 and 2 in Fig. 13h), in contrast to the nnU-Net based segmentation (areas 1 and 2 in Fig. 13 g). Comparing the areas 3 of Fig. 13c) and Fig. 13d), the stitching line artifact is evident for the DB-GAN segmented image, whereas this is not the case for the nnU-Net segmentation. In area 4 of Fig. 13c) and Fig. 13d), both methods have missed the detection of the small damage site, with size around 2 pixels (50 nm), marked by a tiny yellow dot in the ground truth data.

4.1.3. *Generalizability*

A key aspect of machine learning approaches is to investigate their performance on out-of-distribution samples. In particular, we are interested in the performance of the trained networks on new data that does not originate from, for example, the exact same experimental specimen or material that was used to obtain the training data from. In our case, we have applied the trained networks, both for the nnU-Net, as well as the DB-GAN ensemble method, to electron micrographs of the DP800 steel that was subjected to a heat treatment, which changes the microstructure. Compared to the original sample, the martensite islands are finer and more circular, as opposed to more elongated and banded martensite islands in the as-received DP800 sample. A side-by-side comparison of the two microstructures is shown in Fig. 15 with the micrograph in a) taken of the original commercial sheet material that was used to train the networks and the micrograph in b) showing the microstructure after a heat treatment of the original material at 775 °C for 330 s followed by water quenching for martensite formation.

In Fig. 16, we show examples of how either method performs when applied to images obtained from a sample that was not used during network training, i.e. from the new microstructure shown in Fig. 15b. Both methods work well on this previously unseen but visually similar image data. However, again some deficiencies can be seen for both methods on the finest details. If we consider the precision in the detection of the damage sites, the nnU-Net performs better than the DB-GAN ensemble in Fig. 16a) and b). On the other hand, Fig. 16c) and d) show two examples where the GAN-based approach yields better results, whereas nnU-Net fails to identify the complete area of the damage site.

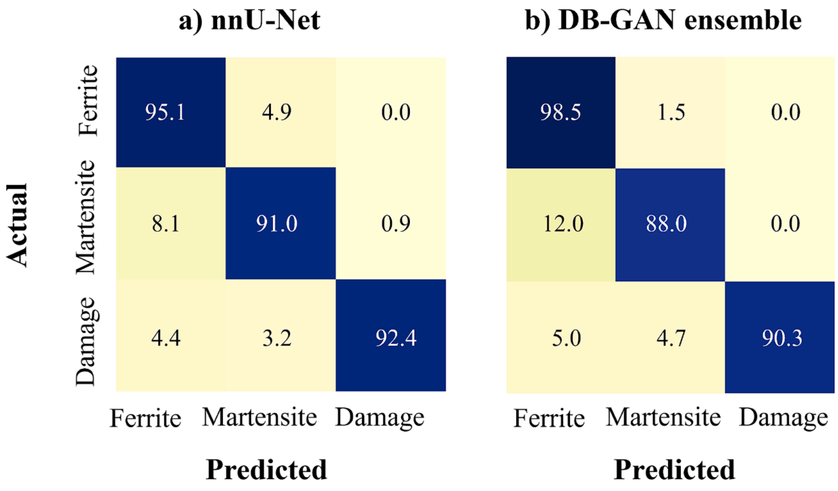

Fig. 12. The average confusion matrix, comparing the performance of the nnU-Net for 512 × 512 pixels images, and DB-GAN ensemble for 250 × 250 pixels images.

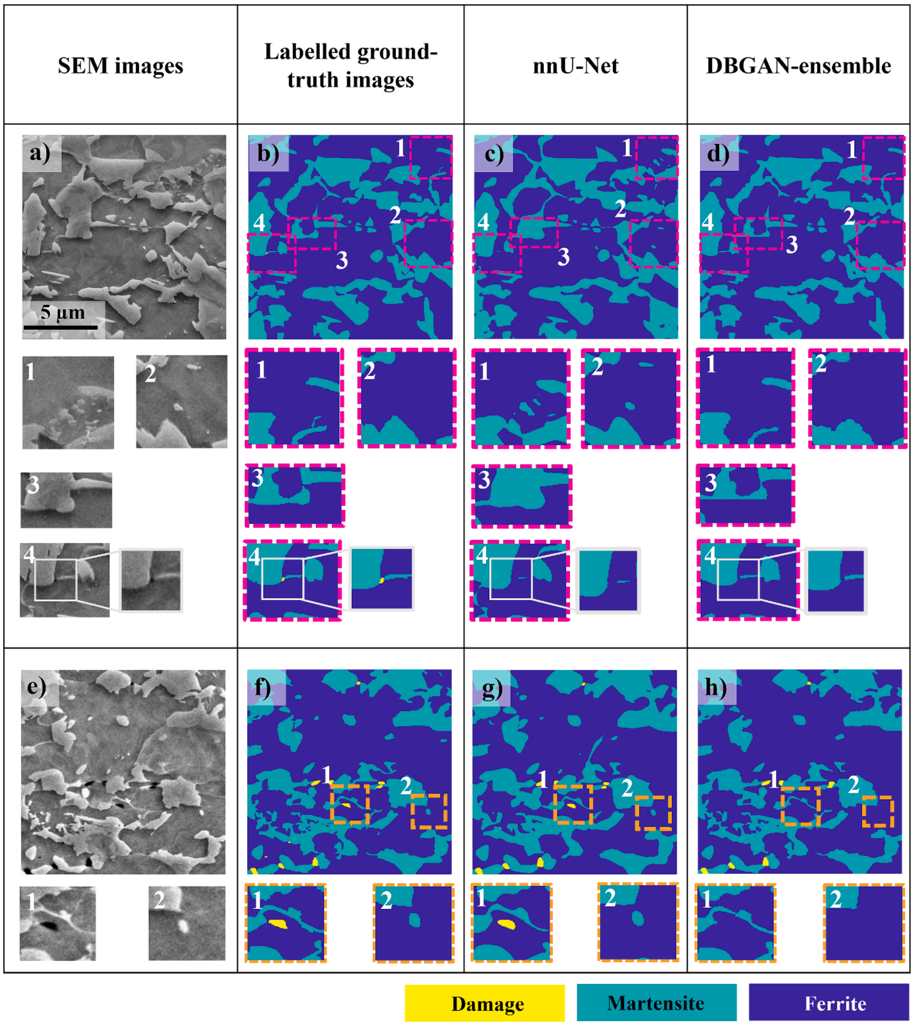

Fig. 13. Examples of SEM images along with the manual labeling, ground truth masks. Side by side comparsion of the images segmented by nnU-Net and DB-GAN ensemble method.

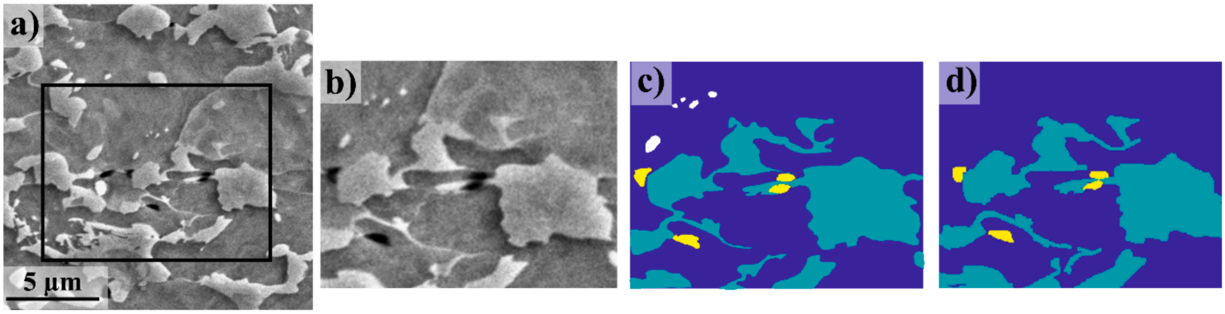

Fig. 14. A) sem image of the microstructure and two different, manually labelled versions of the same image area. b) manual labelling taken directly from the ground truth dataset, c) area relabelled with higher, pixelwise definition of the existing phases and ops particle as an additional fourth class.

In summary, both methods perform reliably on new microstructural configurations, however both methods can fail to yield perfect results, in particular when there are relatively fine details in the microstructure. A more quantitative assessment would require labelling large areas as additional ground-truth for the second microstructure (after heat-treatment). As this process is very labour intensive, doing so is beyond the scope of this work. It is important to keep in mind, however, that while either method show some challenges in processing the finest details of the microstructure perfectly, human experts would likely show the same, if not worse outcomes when processing large-area micrographs of several hundreds of micros in x- and y- direction.

4.1.4. *Usability for microscopists*

Overall, either approachescan be used for image segmentation, provides accurate results, and generalises well to data not seen during training of the machine learning algorithm. The approach based on nnU-Net is almost fully automated and can be applied as a standardised procedure to new scenarios. Compared to the GAN-based approach

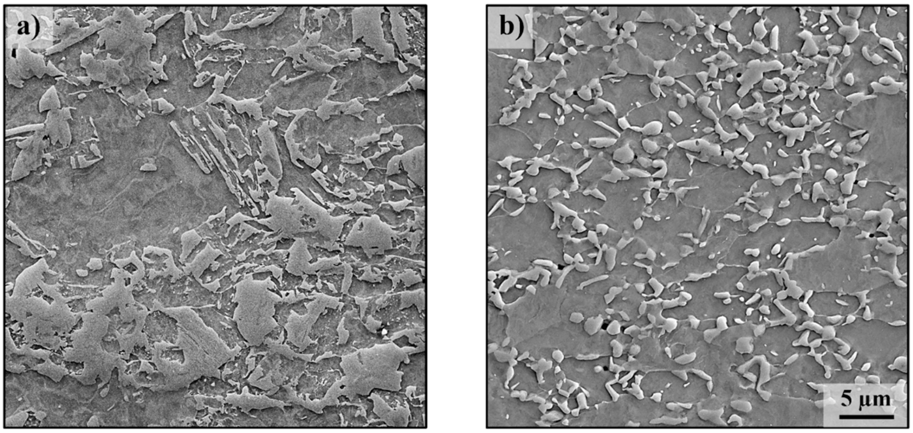

Fig. 15. Comparison of the microstructure configuration of a) the as-received dual phase steel and b) the same steel after heat treatment (775 °C for 330 s followed by water quenching).

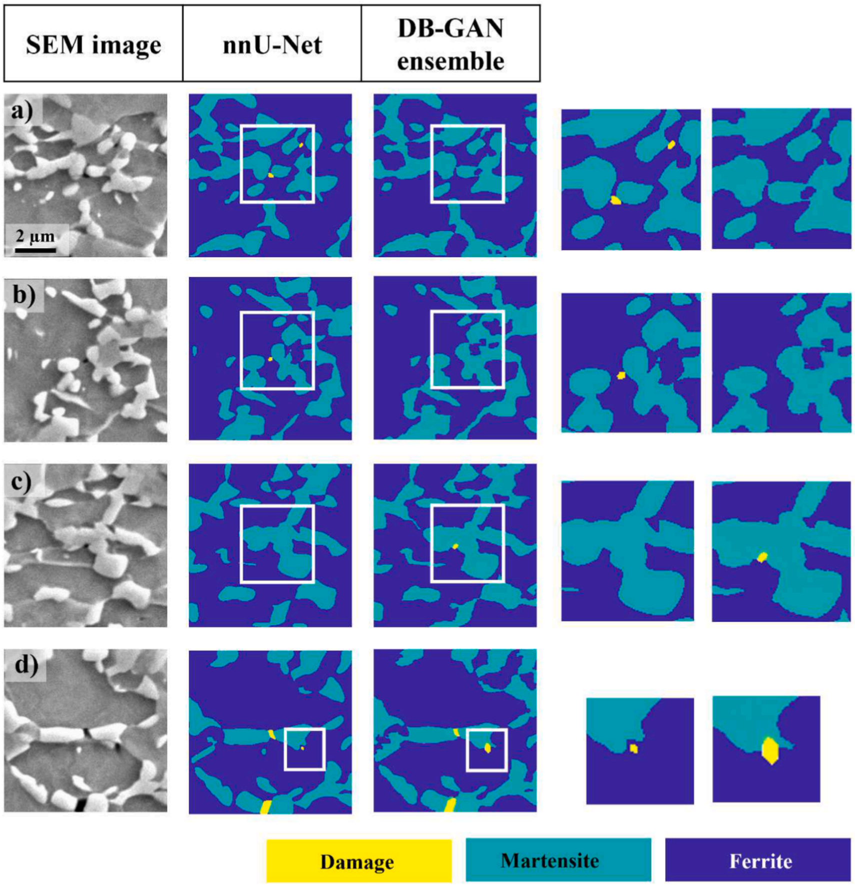

Fig. 16. Comparison of the performance of 2 methods for heat treated dual phase steel (not included within the training data). Images with size equal to training data of DB-GAN ensemble method.

(which achieves its best performance on images of the same size it has been trained on), it can also be applied to larger images, thus avoiding the additional step of cutting and stitching the electron micrographs as part of the procedure. Additionally, further image artefacts due to the stitching of the GAN-segmented images can be avoided.

The DB-GAN ensemble method is much less automated at present and requires several steps, such as, image pre- and postprocessing, cropping and stitching, and potentially correction of associated errors. These extra steps need to be implemented and controlled by the user. The whole process may, therefore, be less convenient for a user interested in fully automated segmentation. However, in some cases the explicit control over individual steps of the segmentation process may be advantageous. We anticipate this to be the case where colour thresholding is of importance. In our case, this was shown to apply where a focus is put on resolving the damage sites accurately, rather than the segmentation of the ferrite and martensite phases that naturally contribute the majority of the imaged surface area. Such intervention in the learning process is more difficult in the nnU-Net method, where changes in performance of the segmentation due to adjusted colour contrast of the input images may equally be expected but iteration towards an improved pre-processing procedure will be much less straightforward.

4.2. Application of large area segmentation 1: Phase fractions in an inhomogeneous dual phase microstructure

A key quantitative parameter in microstructure characterisation is the phase fraction of the constituent phases. The dual phase steel used here as an example, with martensite bands undulating through the sheet metal, presents a particularly challenging case for this, as phase segmentation by simple thresholding is difficult, while manual selection and labelling of small sections can lead to a large variance in the results. In this case, the result will depend strongly on the exact position and size of the windows from which the area fraction was determined.

Using the large-scale segmented images, we can calculate the phase fraction based on a suitably large area, such that the local variations of the microstructure no longer play such a prevalent role. We illustrate this by the following procedure: Choosing nine different window sizes, ranging from approximately 400 μm^2 to 108900 μm^2 (equivalent side lengths are given in Fig. 18), the martensite phase fraction is calculated in each of these windows. We used two different approaches to distribute the windows across the panoramic image: random placement across the panoramic image stipulating zero overlap and placement around nine regularly spaced points of a 3 × 3 grid. The latter allowed us to compare measurements using the entire area of the square panoramic image, while the first gives a more realistic scenario for measurements of area fractions without the use of panoramic imaging. Both approaches are illustrated for selected window sizes in Fig. 17. Random placement was employed up to window size 8 as displayed in Fig. 18.

From these boxes, we calculated the mean and the respective standard deviations for each group of nine windows of equal size. The result is shown in Fig. 18. We can clearly see that the smaller windows show a very large variation, as expected, since these measurements are much more sensitive to the local variation of the microstructure compared to larger windows. This result exemplifies the importance of large and multiarea analysis for quantifying the widely heterogeneous microstructures like the DP800 steel in the current research. The results confirm the possibility of a high fluctuation of the results even for reasonably large areas. This is highlighted here in Fig. 18a) when comparing the measurements for sizes 3 and 4, which may look small considering the illustration in Fig. 17, but correspond to a total measured area of a square with a side length of 183 and 294 μm, respectively. In addition, despite the observed convergence in the determined average martensite phase fraction by increasing the analysed window size, a noticeable dispersion in the values persist at the window size of 330 μm × 330 μm. We note that this represents a large area equal to 1 mm^2 in total for all 9 measurements and therefore would likely be uncommon in past literature for materials such as this DP800 steel, which contains phase detail to the sub-μm scale but cannot be reliably segmented using thresholding across a large area or by using constant settings across many different images. The persistent scatter is therefore likely due to the even larger length-scales of the undulating martensite bands intersecting the surface. A comparison between the size-dependent data for randomly placed windows for phase fraction analysis (sizes 1–8 in Fig. 18a) and the same analysis for regularly arranged, concentric windows (Fig. 18b), underscores this assumption. In the latter case, the distribution of values for each window size appears self-similar and even for the largest window size, each measurement is clearly not representative of the microstructure as a whole. Phase fractions are commonly given as whole %, but without measurements across even larger areas, the minimum size for a reliable measurement that discriminates phase fractions reliably to within 1 % cannot be calculated. In the future, automated panoramic imaging coupled with large area phase segmentation, as presented here, may however help provide

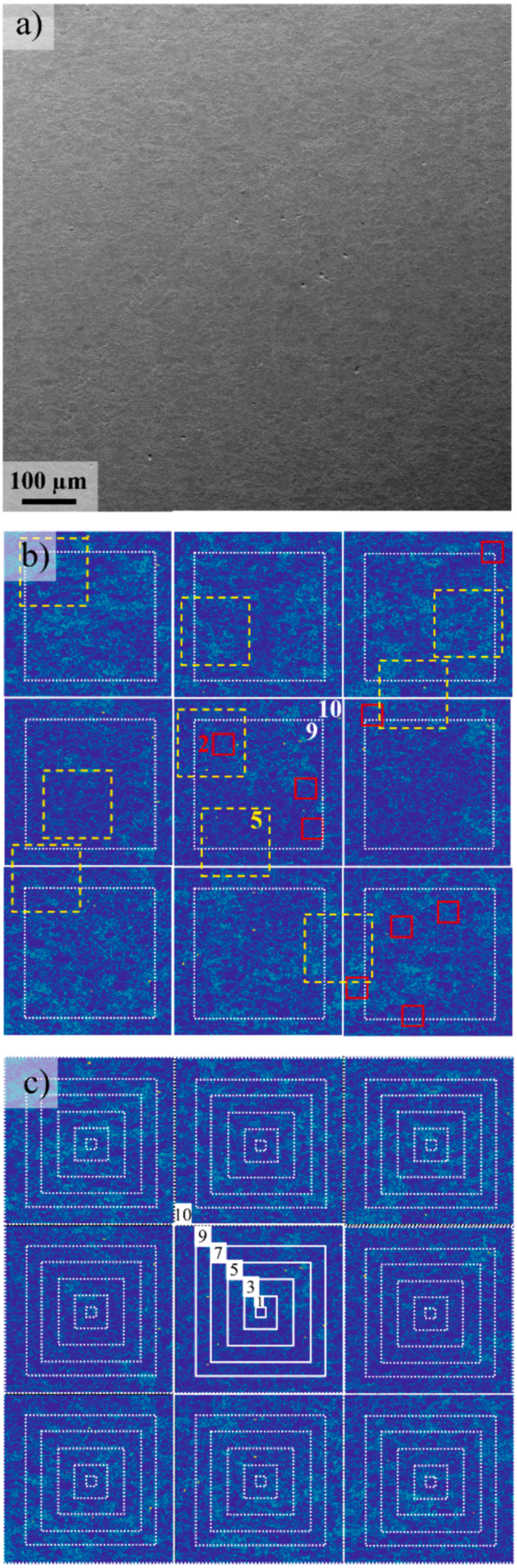

Fig. 17. A) panoramic sem image and segmentation of the image shown in (a). bounding boxes of different size were used for phase fraction calculation and replicated 9 times across the panoramic image either (b) randomly (red and yellow dashed squares) or in b) a regular grid to achieve maximum area without overlap. the numbers given correspond to the sizes given in Fig. 18.

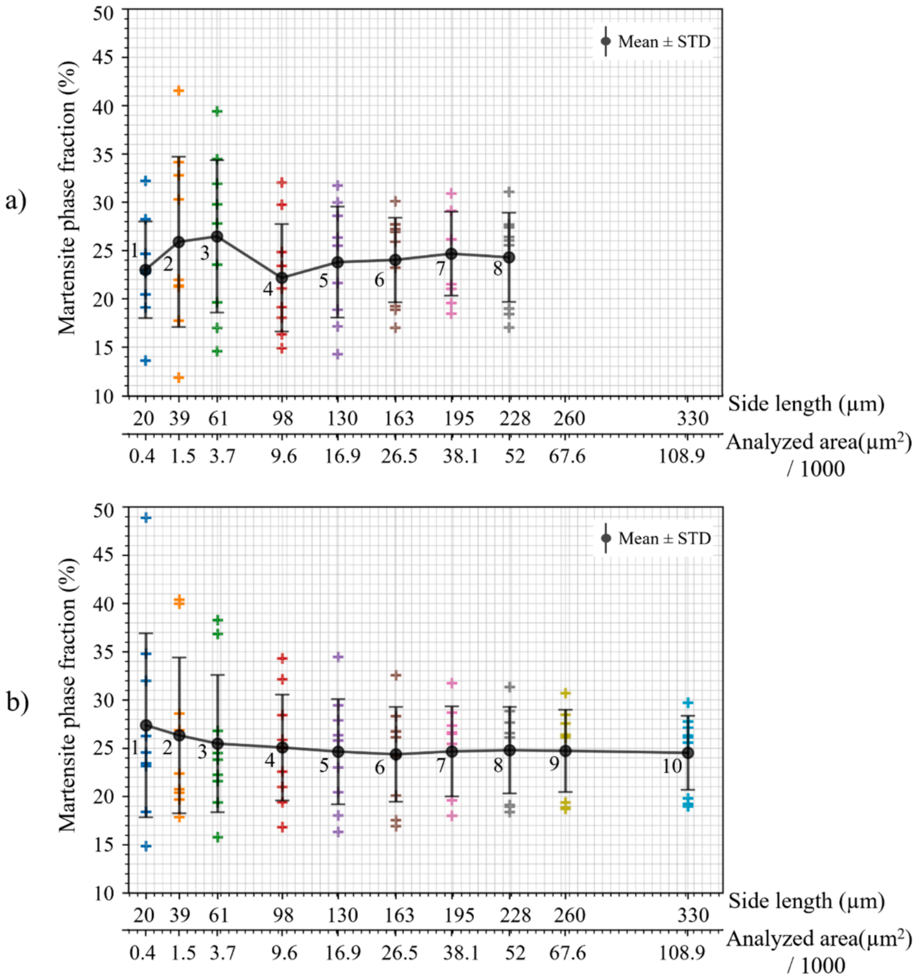

Fig. 18. Area fraction of the martensite phase from 10 different window sizes and using either random (a) or regular (b) spacing of the windows (cf. Fig. 17). Each area fraction is calculated from 9 windows, for which individual values, average and standard deviation are given.

quantifications of microstructure variability to be used instead, e.g. by measuring fluctuations along long line-like scans (instead of the square shape used here) across a surface. In any case our results highlight the fact that martensite phase fraction statements from area measurements using microscopy in dual phase steels may be associated with very large errors that sensitively depend on the underlying area that was evaluated and how this area or segments of the total area measured were placed with respect to long-scale microstructure fluctuations, such as the martensite bands in our dual phase steel. Although this result would appear entirely expected, at least with respect to the deviations between measurements of smaller areas, the majority of publications only state how a phase fraction was measured. They thereby omit the essential information on the total area investigated for this purpose, in spite of the uncertainty of the measurement, which we show here may commonly exceed the accuracy at which the phase fraction measurements are stated and compared.

4.3. Application of large area segmentation 2: Geometric analysis of deformation-induced damage features

In addition to using segmented microstructures for a direct replication in modelling, as exemplified in the previous section, quantitative descriptions of microstructures and features contained therein are often used to study the distribution of features or create representative microstructures for modelling [99,106–110].

The segmented panoramic images of the microstructure presented in this work is particularly suitable for the study of rare or variable features. In the case of the strained dual phase steel, we consider here the geometry of damage sites. As an alternative to performing direct simulations on the segmented microstructures, as exemplified above, average measures of their morphology can also be used to create synthetic microstructures, inform continuum models requiring damage distribution, size or aspect ratio as input, or to assess the spatial distribution of particular types of damage across a sample or in relation to other microstructural features. Here, we will exemplify two applications, namely the investigation of the arrangement of the phases surrounding particular types of damage sites originating from either martensite cracking or interface decohesion and the geometry of these two different classes of damage in terms of their inclination angle to the major strain axis and the void area. For identification of the underlying damage mechanism at the many damage sites contained in a panoramic image, we employed the convolutional neural networks introduced in [30,37] using the unsegmented image data for damage type classification (as the neural networks were not trained on segmented data) and continuing on the same sites using the additional segmentation information obtained here.

Fig. 19 shows an analysis of the angular distribution of the ferrite and martensite phases around interface decohesion (IF) and martensite cracking (MC) sites from around 650 images of each type. The number of the studied damage sites in comparison to similar studies [106] is larger in this work (27 vs. 1300 images) to provide damage sites with variations in the local microstructure. Although there are some similarities in the studied local environment, the use of the segmented microstructures allowed us to extract and quantify the phase distribution around the

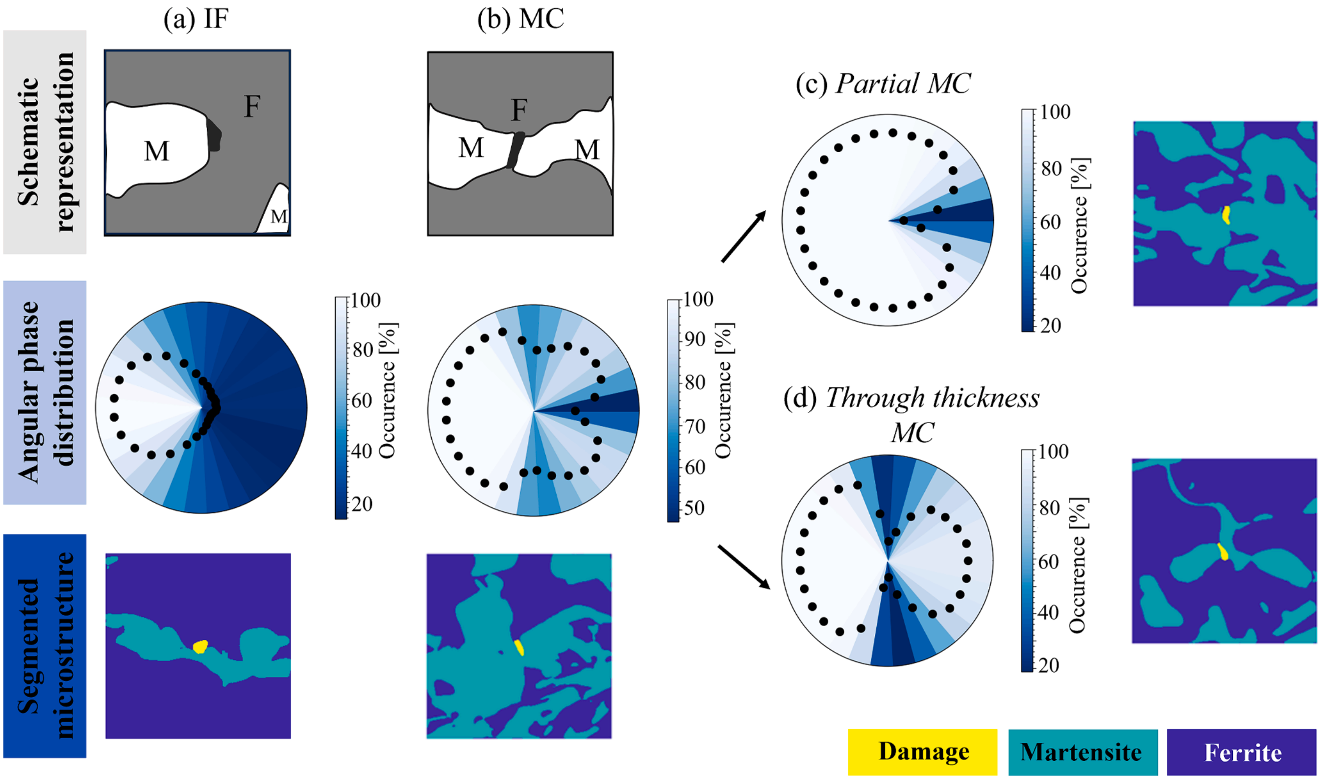

Fig. 19. Angular profile of martensite phase distribution around different types of damage sites. a) Interface decohesion (IF), b) martensite crack (MC). Martensite crack sites comprise two types of cracks partial (c) and through-thickness (d).

damage site. For example, the angular distribution of hard phase is a similar metric to the 2-dimensional distribution of pixel values proposed in the previous investigation [106], while the direct microstructure segmentation ultimately allowed the reduction of the 2-dimensional phase distribution around the damage site to the 1-dimensional angular profile. This distribution also represents a major aspect cited by human researchers in their decision to classify image data of damage sites in dual phase steel [30]. With large area segmentation data now

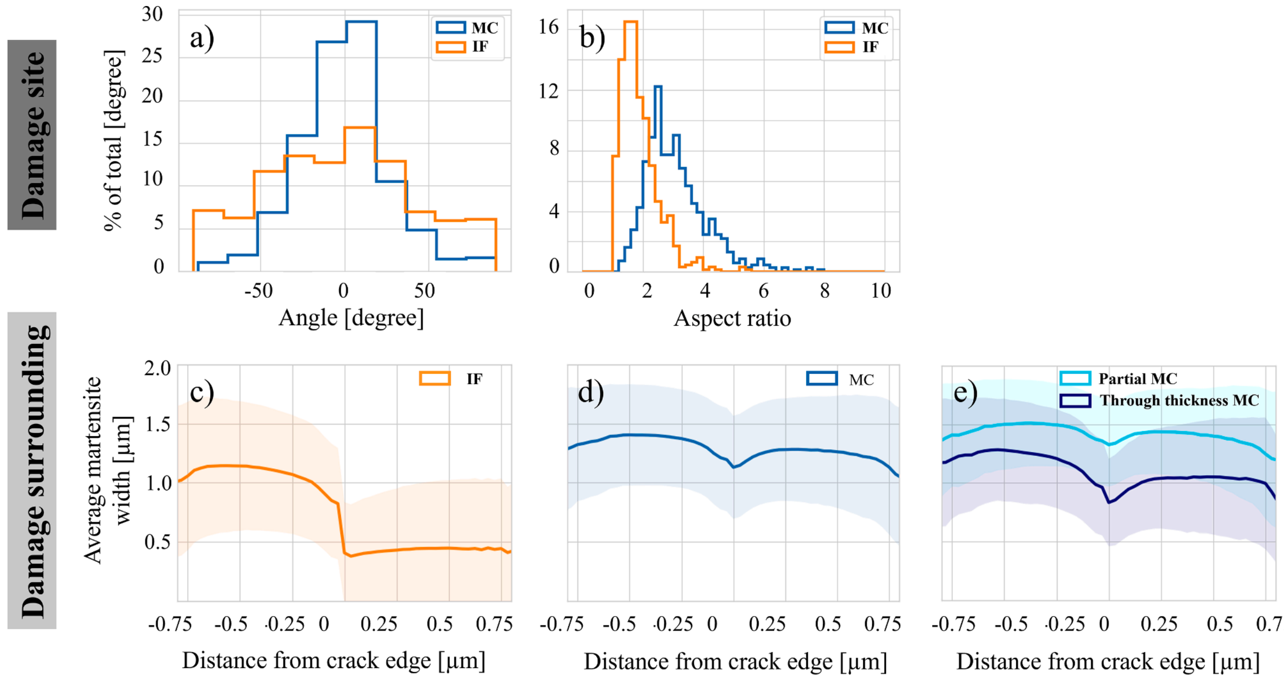

Fig. 20. Distribution of (a) the inclination angle and (b) aspect ratio of two common damage site types (MC: martensite cracking, IF: interface decohesion). The average width of the surrounding martensite for (c) IF and (d) MC sites is shown in terms of the distance from the site/crack edge with the average plotted as full line and the envelope of the corresponding standard deviation highlighted in a lighter shade. In the case of martensite cracks, the data shown in (d) may again be divided into partial and through-thickness cracks (e).

available and encompassing many sites, this kind of data can now be used to formulate a representative geometric signature of the two damage types, in order to circumvent the use of neural networks for damage site classification when using segmented data. Conversely, this analysis may be used to monitor (training) data quality as change in this type of analysis may be expected if different classes of damage sites are inadvertently mixed or if data from very dissimilar microstructures is added. In addition, the geometric analysis may also be of use to introduce a sub-division of a class that was not applied during classification network training. Here, the geometric analysis clearly distinguishes partial and through-thickness cracks, as shown in Fig. 19c and d, respectively. Such a sub-division may, for example, be useful when following crack propagation during in-situ tests as crack nucleation sites that may allow the observation of crack propagation could be easily identified. This analysis can only be achieved by coupling the spatial distribution of the adjacent microstructure with the damage type identified by a human or machine classifier.

Using the spatial phase information extracted from the segmented micrographs enables the extraction of the full geometry of the damage sites, specifically their inclination angle concerning the uniaxial tensile direction, as well as their aspect ratio and the thickness of the martensite area surrounding them, as presented in Fig. 20a (for the methods employed to extract these parameters please refer to the detailed descriptions in the supplementary materials). Although both classes appear to be compatible with a Gaussian distribution, it is evident, that the interface decohesion has a wider distribution and that the martensite cracks are predominantly inclined perpendicular to the loading direction, whereas interface decohesion mechanism does not display a discernible trend. This is in line with the normal stress driven brittle failure of martensite islands and a measure which may change as the stress-state is varied, for example towards biaxial straining [37]. Also consistent with the underlying deformation mechanism, the martensite cracks have a higher tendency to larger aspect ratios, that is a large crack length coupled with smaller crack opening, compared to interface decohesion, which is driven by plastic flow inside the ferrite phase Fig. 20b.

In addition to these fairly obvious observations that may be of use where different strain paths or microstructure morphologies are to be compared, the segmented data may also in the future be used to learn more about an individual mechanism and its relation to the surrounding microstructure. As example, we show here an analysis of the surrounding phase's thickness. Again, the distinction between interface decohesion and martensite cracking reveals the expected tendency, namely that in the case of interface decohesion the martensite island is distributed mainly to one size (cf. Fig. 19) and therefore a larger thickness of martensite is also found towards one side of the crack Fig. 20c. Similarly, martensite cracking is likely to occur at the narrowest point of martensite islands giving a favourable crack path normal to the tensile axis. This is indeed found for the martensite crack here and corresponds to the central minimum of the curve in Fig. 20d. Note that the shaded areas in Fig. 20c-e indicate the standard deviation of the data around the average martensite island width marked with the full line. This implies that for most of the martensite cracks, a local minimum width can be identified at the crack site with most curves showing a shape similar to the average highlighted in a darker shade in Fig. 20c-e. Interestingly, there is again a visible separation between the partial and through-thickness cracks, as plotted in Fig. 20e. The larger thickness reduction around the crack in through-thickness cracks may be the result of martensite plasticity during crack propagation or a pre-existing, stronger constriction of the island favouring crack propagation through the entire thickness of the island. Island thickness may also play a role in addition to any stress concentrating features, as revealed by a tendency of through-cracks to be found in thinner islands, consistent with accelerated crack growth as the process zone of the crack exceeds the fracturing volume. While we cannot draw definite conclusions on this matter based on the data presented here, a careful geometric analysis of martensite island shape and any deformation-induced changes in undeformed and deformed dual phase steel may directly contribute to current research questions surrounding martensite plasticity in dual phase steels. Extending the present work towards detailed EBSD based investigations, which would integrate local orientation information of the phases into the current analysis, may provide an even deeper understanding of the underlying damage mechanisms. For example, by collecting orientation data from many martensite islands, statistically relevant and more direct data on the role of martensite laths and martensite plasticity [111–113] may be acquired for different deformation conditions, alloy compositions, heat treatments or variations in the immediate phase distribution and morphology.

Overall, we show here that segmentation may play an important role in assessing microstructural features and interpreting their occurrence and correlation with other physical mechanisms like deformation-induced damage formation. Machine learning based image segmentation of large panoramic data may now also serve as an alternative approach to side-step detection and classification of microstructural features, such as damage sites of different types [30], which was not possible previously based on the microscopy data alone. Conversely, where machine learning algorithms for classification of microstructural features have already progressed to high maturity or large training datasets have been generated, subsequent segmentation may still be of use to monitor changing training data sets where a hypothesis about feature shape or the distribution of surrounding phases can be formulated. Additionally, recent investigations have developed some automatic machine learning based low dimensional descriptors to establish microstructure-property relationships for microstructures with complex morphologies [109].

4.4. *Application of large area segmentation 3: Microstructure data for modelling*

It is well established that finite element simulations can be used to analyse the properties of a given microstructure numerically, such as, for example, to derive a stress or strain map of the material [114]. However, as a prerequisite, one either needs to employ measures that allow the creation of meaningful synthetic microstructures or, alternatively, "convert" experimental microstructural data into a suitable numerical representation. Here, we again exploit the capabilities of the nnU-Net segmentation algorithm to analyse a large panoramic electron micrograph, which allows us to either model a large area or extract many smaller simulation sites for the same experimental sample and conditions featuring specifically or randomly selected sites, as illustrated in Fig. 21.

Any in-depth discussion or application of different modelling approaches are beyond the scope of this work, however, we note that segmented microstructural images from large areas may be important for modelling of microstructures that vary at different length scales as they enable a free choice of simulation cell size to capture the desired features and processes at small scales, e.g. damage nucleation at individual phase boundaries, and also allow scaling on the same underlying experimental data to capture phenomena at larger scale, such as the coalescence of many damage sites [116]. At the same time, they side-step the need for feature generation, e.g. again by generative machine learning methods, which is fraught with its own challenges and requires additional training and quality control.

5. Conclusions

In this work, we have introduced two new methods for microstructure segmentation based on artificial intelligence with a focus on applying these to large-scale panoramic electron micrographs. As a case-study, we used a commercial dual-phase steel that is used in a wide range of applications but challenging to segment. Both methods show good performance and can be used for segmenting panoramic electron

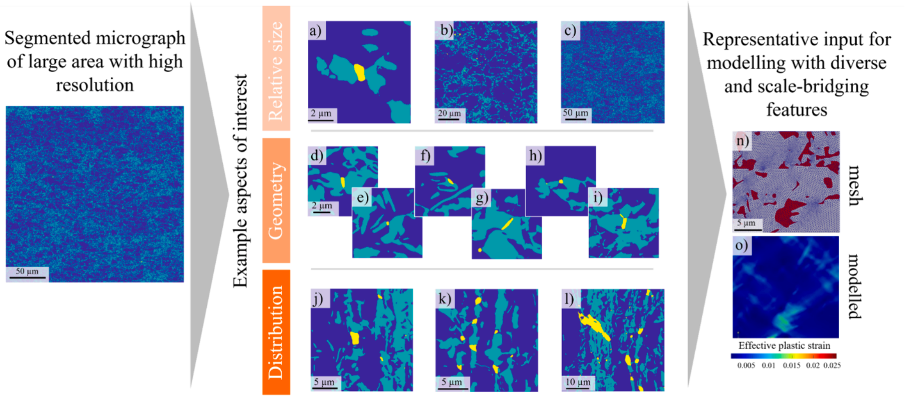

Fig. 21. Illustration of the use of segmented images for modelling of representative features in terms of their size relative to other microstructural components (a-c), different geometries (d-i), or variable distributions within the surrounding microstructure (j-l). Example of finite element mesh (n) and strain calculation (o) using electron micrographs of dual phase steel segmented by the authors taken from [115] distributed under the terms of a Creative Commons CC BY license.

microscope images. A detailed side-by-side comparison of the methods and their applications lead to the following conclusions:

i. Both the nnU-Net and DB-GAN ensemble methods exhibit effective segmentation capabilities for electron micrographs on a large scale, showcasing a high degree of generalizability.
ii. At similar image resolutions, both methods demonstrate comparable pixel-by-pixel accuracy.
iii. Where a high degree of in-built automation is of essence, the nnU-Net method is preferred, as it segments panoramic images directly without the need for the user to crop or stitch panoramic data.
iv. In contrast, the DB-GAN ensemble method involves external cropping and stitching. This comes at the cost of additional pre-processing steps and potential artefacts but may be beneficial where different pre-processing methods or parameters are to be evaluated.
v. Segmentation of microstructures with heterogeneity from the sub-µm to mm-scale scales enables easy area fraction measurements across large panoramic images. Our results also highlight the uncertainty of such measurements and the importance of choosing and stating the considered image size and placement carefully.
vi. The segmented and therefore discretized microstructure also provides data that can be directly used as input for modelling at the microstructural scale and allows the extraction of detailed geometric data about many features, such as deformation-induced damage sites and how these relate to the surrounding phase distribution.

CRediT authorship contribution statement

Setareh Medghalchi: Writing – review & editing, Writing – original draft, Visualization, Validation, Supervision, Methodology, Investigation, Formal analysis, Data curation, Conceptualization. **Joscha Kortmann:** Writing – original draft, Methodology, Investigation, Data curation. **Sang-Hyeok Lee:** Writing – original draft, Visualization, Methodology, Investigation, Formal analysis, Data curation. **Ehsan Karimi:** Visualization, Methodology, Investigation. **Ulrich Kerzel:** Writing – review & editing, Writing – original draft, Validation, Supervision. **Sandra Korte-Kerzel:** Writing – review & editing, Writing – original draft, Supervision, Funding acquisition, Conceptualization.

Declaration of competing interest

The authors declare the following financial interests/personal relationships which may be considered as potential competing interests: Sandra Korte Kerzel reports financial support was provided by Deutsche Forschungsgemeinschaft. Sandra Korte Kerzel reports financial support was provided by Collaborative Research Center TRR 188 (project ID 278868966). Sandra Korte Kerzel reports financial support was provided by Federal Ministry of Education and Research (BMBF). Acknowledgments to Deutsche Forschungsgemeinschaft through projects B2 and T02 of the Collaborative Research Center TRR 188 (project ID 278868966). This work is also funded by the Federal Ministry of Education and Research (BMBF) and the state of North Rhine-Westphalia as part of the NHR Program. Calculations were performed with computing resources granted by RWTH Aachen University under project rwth0535. If there are other authors, they declare that they have no known competing financial interests or personal relationships that could have appeared to influence the work reported in this paper.

Data availability

The segmentation codes, data including trained models, and characterized damage sites are publicly available for use by other researchers at https://doi.org/10.5281/zenodo.11224127 [117].

Acknowledgment

The authors gratefully acknowledge funding by the Deutsche Forschungsgemeinschaft through projects B2 and T02 of the Collaborative Research Centre TRR 188 (project ID 278868966). This work is also funded by the Federal Ministry of Education and Research (BMBF) and the state of North Rhine-Westphalia as part of the NHR Program. Calculations were performed with computing resources granted by RWTH Aachen University under project rwth0535. We further thank Professor Dr. H. Springer for providing the heat-treated samples as well as Mr. M. A. Wollenweber and Dr. Carl F. Kusche for providing the SEM image of cross-sectioned samples and from in-situ deformation experiments.

Appendix A. Supplementary data

Supplementary data to this article can be found online at https://doi.org/10.1016/j.matdes.2024.113031.

References

[1] F.N. Rhines, Microstructure-property relationships in materials, Metall. Trans. A 8 (1977) 127–133.
[2] IEA, Iron and Steel Technology Roadmap—Towards More Sustainable Steelmaking, (2020).

[3] M. Benakis, D. Costanzo, A. Patran, Current mode effects on weld bead geometry and heat affected zone in pulsed wire arc additive manufacturing of Ti-6-4 and Inconel 718, J. Manuf. Process. 60 (2020) 61–74.

[4] H. Xu, Y. Li, C. Brinson, W. Chen, A descriptor-based design methodology for developing heterogeneous microstructural materials system, J. Mech. Des. 136 (5) (2014).

[5] T.M. Nunes, V.H.C. De Albuquerque, J.P. Papa, C.C. Silva, P.G. Normando, E. P. Moura, J.M.R. Tavares, Automatic microstructural characterization and classification using artificial intelligence techniques on ultrasound signals, Expert Syst. Appl. 40 (8) (2013) 3096–3105.

[6] U. Adiga, M. Gorantla, J. Scott, D. Banks, Y.-S. Choi, Building 3d microstructure database using an advanced metallographic serial sectioning technique and robust 3d segmentation tools, Proceedings of the 2nd World Congress on Integrated Computational Materials Engineering (ICME), Springer, 2013, pp. 243-248.

[7] J. Dargay, D. Gately, M. Sommer, Vehicle ownership and income growth, worldwide: 1960–2030, Energy J. 28 (4) (2007).

[8] H. Peregrina-Barreto, I.R. Terol-Villalobos, J.J. Rangel-Magdaleno, A.M. Herrera-Navarro, L.A. Morales-Hernández, F. Manríquez-Guerrero, Automatic grain size determination in microstructures using image processing, Measurement 46 (1) (2013) 249–258.

[9] P. Shi, M. Duan, L. Yang, W. Feng, L. Ding, L. Jiang, An improved U-net image segmentation method and its application for metallic grain size statistics, Materials (basel) 15 (13) (2022).

[10] X. Li, X. Ma, S. Subramanian, C. Shang, R. Misra, Influence of prior austenite grain size on martensite–austenite constituent and toughness in the heat affected zone of 700 MPa high strength linepipe steel, Mater. Sci. Eng. A 616 (2014) 141–147.

[11] J. Tiley, G. Viswanathan, R. Srinivasan, R. Banerjee, D. Dimiduk, H. Fraser, Coarsening kinetics of γ' precipitates in the commercial nickel base Superalloy René 88 DT, Acta Mater. 57 (8) (2009) 2538–2549.

[12] S. Liu, Y.C. Shin, Additive manufacturing of Ti6Al4V alloy: A review, Mater. Des. 164 (2019) 107552.

[13] J.P. MacSleyne, J.P. Simmons, M. De Graef, On the use of 2-D moment invariants for the automated classification of particle shapes, Acta Mater. 56 (3) (2008) 427–437.

[14] J. Villavicencio, N. Ulloa, L. Lozada, M. Moreno, L. Castro, The role of non-metallic Al2O3 inclusions, heat treatments and microstructure on the corrosion resistance of an API 5L X42 steel, J. Mater. Res. Technol. 9 (3) (2020) 5894–5911.

[15] I. Konovalenko, P. Maruschak, O. Prentkovskis, R. Junevičius, Investigation of the rupture surface of the titanium alloy using convolutional neural networks, Materials 11 (12) (2018) 2467.

[16] S. Tsopanidis, R.H. Moreno, S. Osovski, Toward quantitative fractography using convolutional neural networks, Eng. Fract. Mech. 231 (2020) 106992.

[17] T. Falk, D. Mai, R. Bensch, Ö. Çiçek, A. Abdulkadir, Y. Marrakchi, A. Böhm, J. Deubner, Z. Jäckel, K. Seiwald, U-Net: deep learning for cell counting, detection, and morphometry, Nat. Methods 16 (1) (2019) 67–70.

[18] T.C. Hollon, B. Pandian, A.R. Adapa, E. Urias, A.V. Save, S.S.S. Khalsa, D. G. Eichberg, R.S. D'Amico, Z.U. Farooq, S. Lewis, Near real-time intraoperative brain tumor diagnosis using stimulated Raman histology and deep neural networks, Nat. Med. 26 (1) (2020) 52–58.

[19] M. Cheriet, J.N. Said, C.Y. Suen, A recursive thresholding technique for image segmentation, IEEE Trans. Image Process. 7 (6) (1998) 918–921.

[20] K.V. Mardia, T. Hainsworth, A spatial thresholding method for image segmentation, IEEE Trans. Pattern Anal. Mach. Intell. 10 (6) (1988) 919–927.

[21] D. Kim, S. Lee, W. Hong, H. Lee, S. Jeon, S. Han, J. Nam, Image segmentation for FIB-sem serial sectioning of a Si/C–graphite composite anode microstructure based on preprocessing and global thresholding, Microsc. Microanal. 25 (5) (2019) 1139–1154.

[22] V.S.S.A. Karra, A.K. Verma, A. Guzel, A. Huck, A.D. Rollett, Quantification of alpha lath in Ti-6Al-4V using OpenCV, Mater Charact 186 (2022) 111802.

[23] F.Y. Shih, S. Cheng, Automatic seeded region growing for color image segmentation, Image Vis. Comput. 23 (10) (2005) 877–886.

[24] R. Adams, L. Bischof, Seeded region growing, IEEE Trans. Pattern Anal. Mach. Intell. 16 (6) (1994) 641–647.

[25] S. Beucher, F. Meyer, The morphological approach to segmentation: the watershed transformation, Mathematical morphology in image processing, CRC Press, 2018, pp. 433–481.

[26] S.S. Al-Amri, N. Kalyankar, S. Khamitkar, Image segmentation by using edge detection, International Journal on Computer Science and Engineering 2 (3) (2010) 804–807.

[27] S. Savant, A review on edge detection techniques for image segmentation, International Journal of Computer Science and Information Technologies 5 (4) (2014) 5898–5900.

[28] G.B. Coleman, H.C. Andrews, Image segmentation by clustering, Proceedings of the IEEE 67 (5) (1979) 773–785.

[29] S.M. Azimi, D. Britz, M. Engstler, M. Fritz, F. Mücklich, Advanced steel microstructural classification by deep learning methods, Sci. Rep. 8 (1) (2018) 2128.

[30] C. Kusche, T. Reclik, M. Freund, T. Al-Samman, U. Kerzel, S. Korte-Kerzel, Large-area, high-resolution characterisation and classification of damage mechanisms in dual-phase steel using deep learning, PLoS One 14 (5) (2019) e0216493.

[31] T. Strohmann, K. Bugelnig, E. Breitbarth, F. Wilde, T. Steffens, H. Germann, G. Requena, Semantic segmentation of synchrotron tomography of multiphase Al-Si alloys using a convolutional neural network with a pixel-wise weighted loss function, Sci. Rep. 9 (1) (2019) 19611.

[32] R. Lorenzoni, I. Curosu, S. Paciornik, V. Mechtcherine, M. Oppermann, F. Silva, Semantic segmentation of the micro-structure of strain-hardening cement-based composites (SHCC) by applying deep learning on micro-computed tomography scans, Cem. Concr. Compos. 108 (2020) 103551.

[33] E.A. Holm, R. Cohn, N. Gao, A.R. Kitahara, T.P. Matson, B. Lei, S.R. Yarasi, Overview: computer vision and machine learning for microstructural characterization and analysis, Metall. Mater. Trans. A 51 (12) (2020) 5985–5999.

[34] T. Stan, Z.T. Thompson, P.W. Voorhees, Optimizing convolutional neural networks to perform semantic segmentation on large materials imaging datasets: X-ray tomography and serial sectioning, Mater Charact 160 (2020) 110119.

[35] K. Bugelnig, H. Germann, T. Steffens, B. Plank, F. Wilde, E. Boller, G. Requena, Optimized segmentation of the 3D microstructure in cast Al-Si piston alloys, Practical Metallography 55 (4) (2018) 223–243.

[36] F. Ajioka, Z.-L. Wang, T. Ogawa, Y. Adachi, Development of high accuracy segmentation model for microstructure of steel by deep learning, ISIJ Int. 60 (5) (2020) 954–959.

[37] S. Medghalchi, C.F. Kusche, E. Karimi, U. Kerzel, S. Korte-Kerzel, Damage analysis in dual-phase steel using deep learning: transfer from uniaxial to biaxial straining conditions by image data augmentation, JOM 72 (2020) 4420–4430.

[38] S. Medghalchi, E. Karimi, S.-H. Lee, B. Berkels, U. Kerzel, S. Korte-Kerzel, Three-dimensional characterisation of deformation-induced damage in dual phase steel using deep learning, Mater. Des. (2023) 112108.

[39] A.R. Durmaz, M. Muller, B. Lei, A. Thomas, D. Britz, E.A. Holm, C. Eberl, F. Mucklich, P. Gumbsch, A deep learning approach for complex microstructure inference, Nat Commun 12 (1) (2021) 6272.

[40] D. Iren, M. Ackermann, J. Gorfer, G. Pujar, S. Wesselmecking, U. Krupp, S. Bromuri, Aachen-Heerlen annotated steel microstructure dataset, Sci Data 8 (1) (2021) 140.

[41] P.D. Brown, Transmission electron microscopy-A textbook for materials science, by David B. Williams and C. Barry Carter, Microscopy and Microanalysis 5 (6) (1999) 452–453.

[42] B.L. DeCost, B. Lei, T. Francis, E.A. Holm, High throughput quantitative metallography for complex microstructures using deep learning: a case study in ultrahigh carbon steel, Microsc Microanal 25 (1) (2019) 21–29.

[43] A. Thomas, A.R. Durmaz, T. Straub, C. Eberl, Automated quantitative analyses of fatigue-induced surface damage by deep learning, Materials 13 (15) (2020) 3298.

[44] J. Luengo, R. Moreno, I. Sevillano, D. Charte, A. Peláez-Vegas, M. Fernández-Moreno, P. Mesejo, F. Herrera, A tutorial on the segmentation of metallographic images: Taxonomy, new MetalDAM dataset, deep learning-based ensemble model, experimental analysis and challenges, Information Fusion 78 (2022) 232–253.

[45] C. Shen, X. Wei, C. Wang, W. Xu, A deep learning method for extensible microstructural quantification of DP steel enhanced by physical metallurgy-guided data augmentation, Mater Charact 180 (2021) 111392.

[46] T.M. Ostormujof, R.P.R. Purohit, S. Breumier, N. Gey, M. Salib, L. Germain, Deep Learning for automated phase segmentation in EBSD maps. A Case Study in Dual Phase Steel Microstructures, Materials Characterization 184 (2022) 111638.

[47] L. Fu, H. Yu, M. Shah, J. Simmons, S. Wang, Crystallographic symmetry for data augmentation in detecting dendrite cores, Electronic Imaging 32 (14) (2020), 248-1-248-7.

[48] C. Wang, D. Shi, S. Li, A study on establishing a microstructure-related hardness model with precipitate segmentation using deep learning method, Materials 13 (5) (2020) 1256.

[49] N.M. Senanayake, J.L. Carter, Computer vision approaches for segmentation of nanoscale precipitates in nickel-based superalloy IN718, Integrating Materials and Manufacturing Innovation 9 (2020) 446–458.

[50] J. Stuckner, B. Harder, T.M. Smith, Microstructure segmentation with deep learning encoders pre-trained on a large microscopy dataset, npj Comput. Mater. 8 (1) (2022).

[51] N. Lutsey, Review of technical literature and trends related to automobile mass-reduction technology, (2010).

[52] C.C. Tasan, M. Diehl, D. Yan, M. Bechtold, F. Roters, L. Schemmann, C. Zheng, N. Peranio, D. Ponge, M. Koyama, An overview of dual-phase steels: advances in microstructure-oriented processing and micromechanically guided design, Annu. Rev. Mat. Res. 45 (2015) 391–431.

[53] N. Peixinho, N. Jones, A. Pinho, Application of dual-phase and TRIP steels on the improvement of crashworthy structures, Mater. Sci. Forum 502 (2005) 181–188.

[54] A. Mayyas, A. Qattawi, M. Omar, D. Shan, Design for sustainability in automotive industry: A comprehensive review, Renew. Sustain. Energy Rev. 16 (4) (2012) 1845–1862.

[55] S. Medghalchi, M. Zubair, E. Karimi, S. Sandlöbes-Haut, U. Kerzel, S. Korte-Kerzel, Determination of the rate dependence of damage formation in metallic-intermetallic Mg–Al–Ca composites at elevated temperature using panoramic image analysis, Adv. Eng. Mater. 25 (21) (2023) 2300956.

[56] S.Y. Allain, I. Pushkareva, J. Teixeira, M. Gouné, C. Scott, Dual-phase steels: the first family of advanced high strength steels, Elsevier, 2020.

[57] A. Garcia-Garcia, S. Orts-Escolano, S. Oprea, V. Villena-Martinez, P. Martinez-Gonzalez, J. Garcia-Rodriguez, A survey on deep learning techniques for image and video semantic segmentation, Appl. Soft Comput. 70 (2018) 41–65.

[58] A.M. Hafiz, G.M. Bhat, A survey on instance segmentation: state of the art, International Journal of Multimedia Information Retrieval 9 (3) (2020) 171–189.

[59] S. Minaee, Y. Boykov, F. Porikli, A. Plaza, N. Kehtarnavaz, D. Terzopoulos, Image Segmentation Using Deep Learning: A Survey, IEEE Trans Pattern Anal Mach Intell 44 (7) (2022) 3523–3542.

[60] T.M. Inc., MATLAB, Image Labeler application, The MathWorks Inc., Natick, Massachusetts, United States, 2018.

[61] O. Ronneberger, P. Fischer, T. Brox, U-net: Convolutional networks for biomedical image segmentation, Medical Image Computing and Computer-Assisted Intervention–MICCAI 2015: 18th International Conference, Munich, Germany, October 5-9, 2015, Proceedings, Part III 18, Springer, 2015, pp. 234-241.

[62] M. Drozdzal, E. Vorontsov, G. Chartrand, S. Kadoury, C. Pal, The importance of skip connections in biomedical image segmentation, in: International Workshop on Deep Learning in Medical Image Analysis, International Workshop on Large-Scale Annotation of Biomedical Data and Expert Label Synthesis, Springer, 2016, pp. 179–187.

[63] F. Isensee, From Manual to Automated Design of Biomedical Semantic Segmentation Methods, 2020.

[64] F. Sultana, A. Sufian, P. Dutta, Evolution of image segmentation using deep convolutional neural network: A survey, Knowl.-Based Syst. 201 (2020) 106062.

[65] P. Bilic, P. Christ, H.B. Li, E. Vorontsov, A. Ben-Cohen, G. Kaissis, A. Szeskin, C. Jacobs, G.E.H. Mamani, G. Chartrand, The liver tumor segmentation benchmark (lits), Med. Image Anal. 84 (2023) 102680.

[66] N. Heller, F. Isensee, K.H. Maier-Hein, X. Hou, C. Xie, F. Li, Y. Nan, G. Mu, Z. Lin, M. Han, The state of the art in kidney and kidney tumor segmentation in contrast-enhanced CT imaging: Results of the KiTS19 challenge, Med. Image Anal. 67 (2021) 101821.

[67] F. Isensee, P.F. Jaeger, S.A.A. Kohl, J. Petersen, K.H. Maier-Hein, nnU-Net: a self-configuring method for deep learning-based biomedical image segmentation, Nat Methods 18 (2) (2021) 203–211.

[68] A.C. Wilson, R. Roelofs, M. Stern, N. Srebro, B. Recht, The marginal value of adaptive gradient methods in machine learning, Adv. Neural Inf. Proces. Syst. 30 (2017).

[69] Q. Wang, Y. Ma, K. Zhao, Y. Tian, A comprehensive survey of loss functions in machine learning, Annals of Data Science (2020) 1–26.

[70] J. Ma, J. Chen, M. Ng, R. Huang, Y. Li, C. Li, X. Yang, A.L. Martel, Loss odyssey in medical image segmentation, Med. Image Anal. 71 (2021) 102035.

[71] I. Goodfellow, J. Pouget-Abadie, M. Mirza, B. Xu, D. Warde-Farley, S. Ozair, A. Courville, Y. Bengio, Generative adversarial networks, Commun. ACM 63 (11) (2020) 139–144.

[72] M. Mirza, S. Osindero, Conditional generative adversarial nets, arXiv preprint arXiv:1411.1784 (2014).

[73] P. Isola, J.-Y. Zhu, T. Zhou, A.A. Efros, Image-to-image translation with conditional adversarial networks, Proceedings of the IEEE conference on computer vision and pattern recognition, 2017, pp. 1125-1134.

[74] S. Korte-Kerzel, Large-area, high-resolution characterisation and classification of damage mechanisms in dual-phase steel using deep learning, 2019. https://git.rwth-aachen.de/Sandra.Korte.Kerzel/DeepDamage.git.

[75] M. Ester, H.-P. Kriegel, J. Sander, X. Xu, A density-based algorithm for discovering clusters in large spatial databases with noise, kdd, 1996, pp. 226-231.

[76] J.-C. Yen, F.-J. Chang, S. Chang, A new criterion for automatic multilevel thresholding, IEEE Trans. Image Process. 4 (3) (1995) 370–378.

[77] B.C. Cameron, C.C. Tasan, Towards physical insights on microstructural damage nucleation from data analytics, Comput. Mater. Sci 202 (2022) 110627.

[78] F. Bridier, P. Villechaise, J. Mendez, Analysis of the different slip systems activated by tension in a α/β titanium alloy in relation with local crystallographic orientation, Acta Mater. 53 (3) (2005) 555–567.

[79] K.S. Kumar, S. Suresh, M.F. Chisholm, J.A. Horton, P. Wang, Deformation of electrodeposited nanocrystalline nickel, Acta Mater. 51 (2) (2003) 387–405.

[80] A. Tkach, N. Fonshtein, V. Simin'kovich, A. Bortsov, Y.N. Lenets, Fatigue crack growth in a dual-phase ferritic-martensitic steel, Soviet materials science: a transl. of Fiziko-khimicheskaya mekhanika materialov/Academy of Sciences of the Ukrainian SSR 20 (1985) 448-453.

[81] A. Bag, K. Ray, E. Dwarakadasa, Influence of martensite content and morphology on the toughness and fatigue behavior of high-martensite dual-phase steels, Metall. Mater. Trans. A 32 (2001) 2207–2217.

[82] H. Ghadbeigi, C. Pinna, S. Celotto, J. Yates, Local plastic strain evolution in a high strength dual-phase steel, Mater. Sci. Eng. A 527 (18–19) (2010) 5026–5032.

[83] K.K. Alaneme, Fracture Toughness (K1C) evaluation for dual phase medium carbon low alloy steels using circumferential notched tensile (CNT) specimens, Mater. Res. 14 (2011) 155–160.

[84] M. Calcagnotto, Y. Adachi, D. Ponge, D. Raabe, Deformation and fracture mechanisms in fine-and ultrafine-grained ferrite/martensite dual-phase steels and the effect of aging, Acta Mater. 59 (2) (2011) 658–670.

[85] L. Godefroid, M. Andrade, F. Machado, W. Horta, Effect of prestrain and bake hardening heat treatment on fracture toughness and fatigue crack growth resistance of two dual-phase steels, Proceedings of the Materials Science and Technology 2011 Conference, AIST/ASM, 2011.

[86] M. Guan, H. Yu, Fatigue crack growth behaviors in hot-rolled low carbon steels: A comparison between ferrite–pearlite and ferrite–bainite microstructures, Mater. Sci. Eng. A 559 (2013) 875–881.

[87] S. Li, Y. Kang, S. Kuang, Effects of microstructure on fatigue crack growth behavior in cold-rolled dual phase steels, Mater. Sci. Eng. A 612 (2014) 153–161.

[88] A.-P. Pierman, O. Bouaziz, T. Pardoen, P. Jacques, L. Brassart, The influence of microstructure and composition on the plastic behaviour of dual-phase steels, Acta Mater. 73 (2014) 298–311.

[89] S. Sun, M. Pugh, Properties of thermomechanically processed dual-phase steels containing fibrous martensite, Mater. Sci. Eng. A 335 (1–2) (2002) 298–308.

[90] M. Azuma, S. Goutianos, N. Hansen, G. Winther, X. Huang, Effect of hardness of martensite and ferrite on void formation in dual phase steel, Mater. Sci. Technol. 28 (9–10) (2012) 1092–1100.

[91] C. Tian, C. Kirchlechner, The fracture toughness of martensite islands in dual-phase DP800 steel, J. Mater. Res. 36 (2021) 2495–2504.

[92] Q. Lai, O. Bouaziz, M. Gouné, L. Brassart, M. Verdier, G. Parry, A. Perlade, Y. Bréchet, T. Pardoen, Damage and fracture of dual-phase steels: Influence of martensite volume fraction, Mater. Sci. Eng. A 646 (2015) 322–331.

[93] D.L. Steinbrunner, D. Matlock, G. Krauss, Void formation during tensile testing of dual phase steels, Metall. Trans. A 19 (1988) 579–589.

[94] G. Lúcio de Faria, L.B. Godefroid, I.P. Nunes, J. Carlos de Lacerda, Effect of martensite volume fraction on the mechanical behavior of an UNS S41003 dual-phase stainless steel, Mater. Sci. Eng. A 797 (2020).

[95] H. Shen, T. Lei, J. Liu, Microscopic deformation behaviour of martensitic–ferritic dual-phase steels, Mater. Sci. Technol. 2 (1) (1986) 28–33.

[96] M. Ahmadi, M. Sadighi, H.H. Toudeshky, Computational microstructural model of ordinary state-based Peridynamic theory for damage mechanisms, void nucleation, and propagation in DP600 steel, Eng. Fract. Mech. 247 (2021) 107660.

[97] K. Ismail, A. Perlade, P.J. Jacques, T. Pardoen, L. Brassart, Impact of second phase morphology and orientation on the plastic behavior of dual-phase steels, Int. J. Plast 118 (2019) 130–146.

[98] F.M. Al-Abbasi, J.A. Nemes, Micromechanical modeling of the effect of particle size difference in dual phase steels, Int. J. Solids Struct. 40 (13–14) (2003) 3379–3391.

[99] T. De Geus, F. Maresca, R. Peerlings, M. Geers, Microscopic plasticity and damage in two-phase steels: On the competing role of crystallography and phase contrast, Mech. Mater. 101 (2016) 147–159.

[100] C.C. Tasan, J.P. Hoefnagels, M. Diehl, D. Yan, F. Roters, D. Raabe, Strain localization and damage in dual phase steels investigated by coupled in-situ deformation experiments and crystal plasticity simulations, Int. J. Plast 63 (2014) 198–210.

[101] G.A.-F.H. Flower, T. Lindley, Electron backscattering diffraction study of acicular ferrite, bainite, and martensite steel microstructures, Mater. Sci. Technol. 16 (1) (2000) 26–40.

[102] L. Ryde, Application of EBSD to analysis of microstructures in commercial steels, Mater. Sci. Technol. 22 (11) (2006) 1297–1306.

[103] J.Y. Kang, S.J. Park, M.B. Moon, Phase analysis on dual-phase steel using band slope of electron backscatter diffraction pattern, Microsc Microanal 19 (Suppl 5) (2013) 13–16.

[104] F. Zhang, A. Ruimi, D.P. Field, Phase identification of dual-phase (DP980) steels by electron backscatter diffraction and nanoindentation techniques, Microsc. Microanal. 22 (1) (2016) 99–107.

[105] C. Tian, D. Ponge, L. Christiansen, C. Kirchlechner, On the mechanical heterogeneity in dual phase steel grades: Activation of slip systems and deformation of martensite in DP800, Acta Mater. 183 (2020) 274–284.

[106] T.W.J. de Geus, C. Du, J.P.M. Hoefnagels, R.H.J. Peerlings, M.G.D. Geers, Systematic and objective identification of the microstructure around damage directly from images, Scr. Mater. 113 (2016) 101–105.

[107] T. de Geus, M. Cottura, B. Appolaire, R. Peerlings, M. Geers, Fracture initiation in multi-phase materials: A systematic three-dimensional approach using a FFT-based solver, Mech. Mater. 97 (2016) 199–211.

[108] T. De Geus, R. Peerlings, M. Geers, Microstructural topology effects on the onset of ductile failure in multi-phase materials–A systematic computational approach, Int. J. Solids Struct. 67 (2015) 326–339.

[109] N. Kusampudi, M. Diehl, Inverse design of dual-phase steel microstructures using generative machine learning model and Bayesian optimization, Int. J. Plast 171 (2023) 103776.

[110] B.C. Cameron, C.C. Tasan, Microstructural damage sensitivity prediction using spatial statistics, Sci. Rep. 9 (1) (2019) 2774.

[111] C. Du, R. Petrov, M.G.D. Geers, J.P.M. Hoefnagels, Lath martensite plasticity enabled by apparent sliding of substructure boundaries, Mater. Des. 172 (2019).

[112] T. Vermeij, C.J.A. Mornout, V. Rezazadeh, J.P.M. Hoefnagels, Martensite plasticity and damage competition in dual-phase steel: A micromechanical experimental–numerical study, Acta Mater. 254 (2023).

[113] L. Morsdorf, O. Jeannin, D. Barbier, M. Mitsuhara, D. Raabe, C.C. Tasan, Multiple mechanisms of lath martensite plasticity, Acta Mater. 121 (2016) 202–214.

[114] P. Bate, Modelling deformation microstructure with the crystal plasticity finite–element method, Philosophical Transactions of the Royal Society of London Series A: Mathematical, Physical and Engineering Sciences 357 (1756) (1999) 1589–1601.

[115] B. Lin, Data-driven Analysis of Microstructure-Property Relation in Functional Materials, (2023).

[116] C.F. Kusche, F. Pütz, S. Münstermann, T. Al-Samman, S. Korte-Kerzel, On the effect of strain and triaxiality on void evolution in a heterogeneous microstructure–A statistical and single void study of damage in DP800 steel, Mater. Sci. Eng. A 799 (2021) 140332.

[117] S. Medghalchi, Automated Segmentation of Large Image Datasets using Artificial Intelligence for Microstructure Characterisation and Damage Analysis [Data set]. Zenodo. https://doi.org/10.5281/zenodo.11224127.